INTERNATIONAL JOURNAL FOR NUMERICAL METHODS IN FLUIDS
Int. J. Numer. Meth. Fluids 2006; **51**:117–157
Published online 15 November 2005 in Wiley InterScience (www.interscience.wiley.com). DOI: 10.1002/fld.1092

On the interplay between inertial and viscoelastic effects for the flow in weakly modulated channels

Ehab Abu-Ramadan and Roger E. Khayat*,†

Department of Mechanical and Materials Engineering, The University of Western Ontario, London, Ontario, Canada N6A 5B9

SUMMARY

The flow inside a spatially modulated channel is examined for viscoelastic fluids of the Oldroyd-B type. The lower wall is flat and the upper wall is sinusoidally modulated. The modulation amplitude is assumed to be small. Thus, a regular perturbation expansion of the flow field coupled to a variable-step finite-difference scheme is used to solve the problem. Convergence and accuracy assessment against earlier experimental results indicate that there is a significant range of validity of the perturbation approach. The influences of wall geometry, inertia and viscoelasticity on the flow kinematics and stresses are investigated systematically. In particular, the interplay between the flow and fluid parameters effects on the conditions for the onset of backflow, number of vortices, their size and location is revealed. The distance between the flow separation and reattachment locations identifies the vortex size. Non-monotonic dependence of the vortex size on elasticity is reported. The critical conditions for the onset of negative elasticity effects on vortex size are identified. The critical Reynolds number for the onset of backflow initially decreases then levels off or even increases as elasticity increases. For highly elastic fluid and large enough Reynolds number, more than one vortex appear near the lower wall. Copyright © 2005 John Wiley & Sons, Ltd.

KEY WORDS: spatially modulated channels; viscoelastic fluid; Oldroyd-B model; vortex formation; geometric effects; elasticity effects

1. INTRODUCTION

The periodic, modulated channel is a simple geometry with applications in many engineering fluid flow devices. In some instances, the wall modulation is a natural artefact of a machining process, while in other applications, the modulation is incorporated into the design to modify the flow for the purpose of enhanced mixing or heat transfer as encountered in compact, high

*Correspondence to: Roger E. Khayat, Department of Mechanical and Materials Engineering, The University of Western Ontario, London, Ontario, Canada N6A 5B9.
†E-mail: rkhayat@eng.uwo.ca

Contract/grant sponsor: Natural Science and Engineering Council, Canada

Received 28 October 2004
Revised 18 August 2005
Accepted 21 August 2005

flux heat exchangers, and membrane blood oxygenators [1]. The converging–diverging nature of the periodically modulated channels captures the quintessential features of porous media flow, as in the case of tertiary oil recovery, paper and textile coating, composite manufacturing and biological transport processes [2–11]. In spite of the apparent geometrical simplicity, these flows can contain separated flow regions and exhibit many of the features present in much more complex geometries [3, 4, 10–18]. These features can significantly impact heat or mass transfer performance. This richness in physical phenomena in a relatively simple geometry is behind the ongoing fundamental interest. Moreover, this flow configuration provides an ideal setting for the evaluation of constitutive equations [2–4, 18, 19], and for the developing and testing of the accuracy and efficiency of numerical methods in viscoelastic flow calculations [8, 20]. This work aims at analysing viscoelastic effects on the flow through periodically modulated channels numerically.

It is well established experimentally that polymeric flow through porous media is characterized by a substantially higher flow resistance (*pressure drop*) in reference to the purely viscous case [6, 21, 22]. The large increase in the flow resistance is associated with the extensional and elastic effects of the polymeric flow. Due to the similarities between periodically modulated geometries and porous media, viscoelastic flow through modulated channels or tubes is expected to exhibit larger flow resistance in comparison to the purely viscous case. Numerical investigations on viscoelastic flow inside periodically modulated geometries fail to capture the considerable increase in the pressure drop [2–6, 8, 20]. Some researchers have suggested that the failure of theoretical investigations might be attributed to an inherent inadequacy of the modulated geometries to capture the characteristics of porous medium paths. However, clear elastic effects on the increase in flow resistance have been confirmed experimentally for periodically modulated channels or tubes [7, 9, 11]. Furthermore, Talwar and Khomami [23] compared the numerical results for steady flow of polymeric fluids past periodic square arrays of cylinders with the experimental measurements of Skartsis *et al.* [22] with a 2% aqueous polyacrylamide solution. It was shown that the computed and the experimental results are similar below a critical Reynolds number, *Re*, or Weissenberg number, *We*. Above this critical value, the experimental results exhibit a dramatic increase in the flow resistance. Thus, the discrepancy between experimental and numerical results may be related either to the inadequacy of the constitutive model or more likely to the non-linear transition to a different flow structure, which substantially increases the flow resistance. If this transition is due to Hopf or degenerate Hopf bifurcation, the steady numerical computations follow the steady branch of the solution become physically unattainable.

Various constitutive models have been employed to overcome the discrepancy between the numerical and experimental findings [2–5]. Although different viscoelastic models show different flow resistance values when other geometric and flow parameters are unchanged, all of the reported numerical results severely underestimated the flow resistance. Furthermore, there are experimental data [24] obtained with a sinusoidally modulated tube and M1 Boger fluid, which show quantitative agreement with numerically calculated flow resistance values using the Oldroyd-B model and steady-state assumptions. Since these experimental data were obtained at *Re* less than unity and small elasticity values (Deborah number, $De < 3$), the experimental results might represent steady viscoelastic flow. Thus, the deviation between numerical and experimental results is more likely to be attributed to the possibility that the experimental increase in the flow resistance arises from a temporal instability, where the steady two-dimensional flow exhibits a non-linear transition to another three dimensional or time

periodic or non-axially periodic flow structure that considerably increase the flow resistance. Temporal instability as the most logical reason behind the abrupt increase in the flow resistance is strongly supported by another two experimental studies [25, 26]. Both of those studies suggest that purely elastic flow loses its stability above a critical *We* and the transition is due to Hopf bifurcation. Therefore, stability analysis of a typical viscoelastic fluid flow inside modulated geometries is important to understand the deviation between experimental and numerical results.

Given the complexity of the geometries and the non-linearities involved (of elastic and inertial nature), linear or non-linear stability analysis is too stiff for a numerical stability investigation to be preformed. It was stated by Pilitsis and Beris [3] that the mixed pseudospectral/finite difference technique is not suitable for time-dependent calculations. Although Sureshkumar [27] attempted to investigate the linear stability of sinusoidally periodic channel flow using an upper convected Maxwell (UCM) model in the inertial and purely elastic region, his technique seems to underestimate the critical Reynolds number for the onset of instability even in the Newtonian limit (see Fig. 20 in Reference [14]). Due to the numerical difficulties associated with establishing reliable numerical stability analysis for viscoelastic fluid flows inside modulated geometries, it is advisable to investigate the temporal stability analysis *experimentally*. However, one has to establish, *numerically*, first the influence of fluid and geometric parameters on the steady flow structure of viscoelastic fluids inside modulated geometries. The numerically calculated results will then be compared against the experimentally observed ones to locate the critical conditions where the steady branch of the numerical solutions becomes physically unattainable. The current work is only limited to investigate steady viscoelastic flow inside modulated channels numerically.

One has to be careful in selecting the appropriate constitutive model to efficiently describe the experimentally employed viscoelastic fluid. Davidson *et al.* [17, 19] illustrated that the deviation between the numerically calculated and the experimentally measured flow kinematics for the flow of 20% polystyrene solution in a periodically constricted channel may be due to the inadequacy of using the UCM or White-Metzner model to describe such fluid. Doyle *et al.* [28] have shown that a dilute monodisperse polystyrene solution exhibits a stress-conformation hysteresis. That is, the stress and the end-to-end conformation evolve along one path during the transient unraveling process and a distinct second path during the relaxation back to equilibrium. Such hysteretic effects cannot be captured with simple dumbbell models like the UCM or the White-Metzner model, but at least qualitatively by simple closed-form constitutive models such as the ones proposed by Hinch [29] and Rallison [30].

Hardly any work has been preformed to examine the influence of polymeric flow parameters on the velocity and stress fields in complex geometries in the inertial regime. The motivation behind most of the reported studies was to investigate elastic effects on the flow resistance. The flow inside periodic, modulated channel or tube exhibits an abundance of interesting physics depending upon the modulation amplitude and frequency, and the flow rate of the passing fluid. For Newtonian fluid, numerical results and experimental flow visualizations showed that recirculation regions, often referred to as vortices, would form beneath the modulation crest beyond a certain *critical* Reynolds number that decreases exponentially as the modulation amplitude or the wavenumber increases [1, 12–15, 31–38]. The size of the recirculation flow region as identified by the distance between the separation and reattachment points varies with Reynolds number as *Re* increases beyond the critical Reynolds number. The interested reader is referred to Zhou *et al.* [13, 14] for a comprehensive review of the pertinent literature.

Influence of viscoelasticity on the conditions for the onset of separation, number of vortices, their size and location has never been systematically examined. While few examples [3, 20] have been reported where an increase in elasticity causes a reduction in the vortex size, other studies [39, 40] demonstrate that an increase in elasticity results in a simultaneous vortex growth. Elasticity contradictory effects may be related to the inconsistency in the examined flow parameters and geometric modulation amplitudes and frequencies among various studies. A relation among flow and geometric parameters to estimate a critical elasticity value beyond which elasticity has a negative effect on vortex formation should exist. Since there is no systematic study on the interplay between viscoelastic fluid and geometric parameters effects on vortex formation, the critical elasticity value has not been determined yet. One of the main objectives of the current study is to estimate this critical value numerically.

Numerical analysis of viscoelastic flow through periodically modulated channels or tubes is significantly complicated, primarily because of the non-linearities and the hyperbolic-like character of the governing equations. King *et al.* [41] have used a restructured form of the momentum equations (explicitly elliptic form of the momentum equations, EEME) for the steady creeping flow calculation of UCM model in smooth and singular geometries in order to overcome the difficulties with obtaining convergent numerical solutions for steady viscoelastic flows using straightforward application of finite element or finite difference methods. The restructured problem was solved by the Galerkin finite element method. Since this method is restricted to creeping UCM model, it is not advisable to be employed here to investigate the interplay between inertia and viscoelastic effects. Although Phan-Thien and Khan [7] managed to obtain a numerically stable solution for the flow of Oldroyd-type fluid through a sinusoidal tube using the boundary element method, their results are unreliable because of the employment of too coarse mesh. Upon using a finer mesh, the boundary element method results resembled a better agreement with other numerical methods [8]. Other than the larger CPU cost associated with the employment of finer mesh, the validity of the boundary element method is questionable because of the development of a steep stress gradients near the walls [2, 3].

A more powerful approach that combines the high accuracy of the spectral method and the computational efficiency of finite element/finite difference techniques is the mixed pseudo-spectral/finite difference approach [2]. Although this method managed to provide accurate results without increasing the computational domain [8, 20, 42], it experiences some difficulties in handling flow with recirculation, especially when inertia is present. Recirculation regions were predicted only for large amplitude modulation and creeping flow [3]. In addition, a special modification to the method has to be implemented to examine Oldroyd-B model rather than the UCM. Since the current study examines the intricate interaction between inertia and viscoelastic effects on the conditions for onset of backflow in the limit of small modulation, the pseudospectral/finite difference method may be unsuitable.

Another numerically stable approach is the perturbation approach. The accuracy of this approach depends on the amplitude of the modulation. This approach is of interest because of its simplicity and the fact that in many applications, the interest lies in small modulation where the perturbation method provides reasonable accuracy. In fact, the perturbation approach has been used by Beris *et al.* [2, 3, 5] to estimate the accuracy of the pseudospectral/finite difference technique. Ahrens *et al.* [43] used the undulating tube geometry and a first-order domain perturbation analysis to investigate the change of type occurring in the vorticity equation from elliptic to hyperbolic at high Reynolds number for an Oldroyd-type fluid. In order to overcome

the difficulties associated with imposing boundary conditions over irregular boundaries, Zhou *et al.* [13] suggested combining the perturbation approach with the mapping approach, where the physical modulated domain is transformed into a simple rectangular domain. By taking advantage of the mapping approach, one also adopts the essence of the perturbation method to reduce the complicated transformed governing equations into a set of ordinary differential equations subject to simple boundary conditions.

For Newtonian fluid flow inside modulated channels, Zhou *et al.* [13, 14] compared the first-order perturbation results to simulations obtained using finite volume approach [44]. The validity of the finite-volume code itself was established by comparison with the experimental results of Nishamura *et al.* [33, 34]. It was found that the velocity and pressure fields were predicted accurately (to within 1%) for small modulation amplitudes and large wavelengths. The differences in the predicted flow are kept well around the order of the square of the dimensionless amplitude. Abu-Ramadan and Khayat [45] established that the presence of non-Newtonian parameters does not seem to affect the accuracy of the perturbation approach. For purely elastic steady flow, Sureshkumar [27] showed that the maximum flow resistance difference upon using second-order domain perturbation analysis and the more accurate finite element approach is less than 3% for dimensionless wall amplitude, wavenumber and De equal to 0.15, 1, and 4.5, respectively. It is important to address the issue of the convergence rate and storage requirement for any conventional numerical method and the perturbation method. Executing the problem using finite element or finite volume method requires large storage and slow convergence rate. In fact, the domain perturbation analysis is an order of magnitude faster than the finite element or the finite volume method [14, 27]. Since the domain perturbation approach is intended to provide a fast and accurate alternative to conventional numerical methods in the limit of small modulation, second-order perturbation analysis will be implemented here.

The present study aims to correct three apparent deficiencies gleaned from the above literature review. First, although the precision of the perturbation method was established for Newtonian flow [13, 14], the range of validity of the perturbation approach for viscoelastic flow is still relatively unexplored. Second, there has not been any systematic study on the interplay between inertia and viscoelastic effects on the flow characteristic. The reported numerical studies have primarily focused on fluid elasticity effects on the flow resistance. The hydrodynamic features of the steady viscoelastic flow in weakly modulated channels will be described in a systematic and coherent way. The present study emphasizes, particularly, the influence of inertia and viscoelasticity, as well as geometric parameters on the conditions for the onset of backflow, vortex size and location. Third, earlier investigations indicate the existence of a critical elasticity value above which elasticity has a negative effect on vortex formation. This critical value and its relation with other parameters have never been established. Estimating this value numerically is an important part of the current study.

In this study, while the channel lower wall is straight, the upper wall is spatially modulated. This geometry is used in a variety of engineering flow devices, and can capture the features of porous media flow. In order to eliminate shear-thinning effects, Oldroyd-B model will be used. This model describes the rheological behaviour of Boger fluids [46, 47], which are highly elastic viscoelastic fluids with constant viscosity. In the following section, the problem formulation and solution procedure are described. The third section introduces the numerical assessment. Numerical results are presented in the fourth section. Some conclusions are drawn in the fifth section.

2. PROBLEM FORMULATION AND SOLUTION PROCEDURE

In this section, the general equations and boundary conditions for the pressure-driven flow with spatially modulated walls are derived for small-amplitude modulation. A regular perturbation expansion for the flow field is carried out after the equations are mapped over a rectangular domain, reducing the problem to a set of ordinary differential equations, which will be solved using a variable-step-finite-difference scheme.

2.1. Governing equations

Consider the flow of an incompressible viscoelastic fluid of density ρ, relaxation time Λ, and viscosity μ. In this study, only fluids that can be reasonably represented by a single relaxation time and constant viscosity are considered. The fluid is assumed to be pressure driven between two infinite rigid boundaries, where the upper wall only is arbitrarily but periodically modulated. The analysis is confined to a two-dimensional steady state flow. Typically, the examined fluid is a polymer solution composed of a Newtonian solvent and a polymer solute of viscosities μ_s and μ_p, respectively. Thus, the viscosity of the solution is given by $\mu = \mu_s + \mu_p$.

The problem is first introduced in the (X, Y) plane, with the X-axis coinciding with the lower wall. The general shapes of the lower and upper boundaries are thus given by $Y = 0$ and $Y = D + Af(X)$, respectively, where A is the modulation amplitude, and D is the mean gap width. Here $f(X)$ is a general function of X that may be arbitrarily prescribe. In this work, however, only a sinusoidal modulation will be considered. The periodicity length of the sinusoidal wave is L. Other modulation, such as the arc shape or the triangle modulation can be represented by a general Fourier series as illustrated by Zhou *et al.* [14]. The general shape of the channel is illustrated in Figure 1.

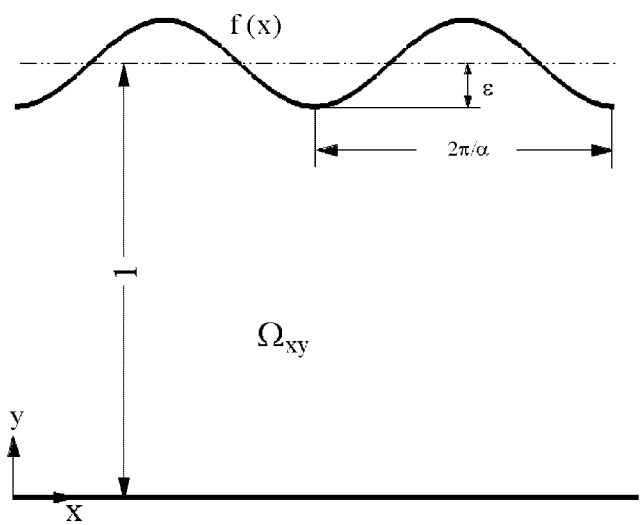

Figure 1. Physical domain for spatially modulated channel (dimensionless notation is used).

The general conservation of mass and linear momentum equations are given by

$$\nabla \cdot \mathbf{U} = 0, \quad \rho(\mathbf{U}\nabla \cdot \mathbf{U}) = -\nabla P + \mu_s \nabla^2 \mathbf{U} + \nabla \cdot \mathbf{T} \tag{1}$$

where ∇ is the gradient operator, $\mathbf{U}(U, V)$ is the velocity vector, P is the pressure, and $\mathbf{T}$ is the elastic part of the deviatoric stress tensor. In this work, the fluid is assumed to obey the Oldroyd-B constitutive model [46] so that $\mathbf{T}$ is governed by

$$\Lambda[\mathbf{U}.\nabla\mathbf{T} - (\nabla\mathbf{U})^t.\mathbf{T} - \mathbf{T}.\nabla\mathbf{U}] = -\mathbf{T} + \mu_p[\nabla\mathbf{U} + (\nabla\mathbf{U})^t] \tag{2}$$

where Λ is the fluid relaxation time, and a superscript, t, donates matrix transposition. The fluid is assumed to adhere to the rigid boundaries, and the no-slip and no-penetration boundary conditions are written as

$$\mathbf{U}(X, Y = 0) = \mathbf{U}(X, Y = D + A f(X)) = 0 \tag{3}$$

It is convenient to cast the problem in terms of dimensionless terms, which are introduced as follows:

$$\begin{gathered}(x, y) = \frac{1}{D}(X, Y), \quad (u, v) = \frac{1}{U_{\max}}(U, V) \\ (Q, R, S) = \frac{D}{\mu U_{\max}}(T_{XX}, T_{YY}, T_{XY}), \quad p = \frac{D}{\mu U_{\max}} P\end{gathered} \tag{4}$$

where $U_{\max}$ is the maximum velocity corresponding to an equivalent linear pressure gradient imposed on the Poiseuille flow between two flat plates coinciding with the mean height of the modulated walls. The subscript, here, donates the direction. After the dimensionless variables are introduced, six important dimensionless groups emerge in the problem, namely, the Reynolds number Re, Deborah number De, solvent-to-solute viscosity ratio Rv, dimensionless wavelength, λ, wavenumber, α, and the aspect ratio ε:

$$\begin{gathered}Re = \frac{\rho U_{\max} D}{\mu}, \quad De = \frac{\Lambda U_{\max}}{D}, \quad Rv = \frac{\mu_s}{\mu_p} \\ \lambda = \frac{L}{D}, \quad \alpha = \frac{2\pi}{\lambda}, \quad \varepsilon = \frac{A}{D}\end{gathered} \tag{5}$$

The dimensionless conservation equations are:

$$u_x + v_y = 0 \tag{6a}$$

$$Re(uu_x + vu_y) = -p_x + aRv(u_{xx} + u_{yy}) + Q_x + S_y \tag{6b}$$

$$Re(uv_x + vv_y) = -p_y + aRv(v_{xx} + v_{yy}) + S_x + R_y \tag{6c}$$

whereas the constitutive equation (2) becomes:

$$De[uQ_x + vQ_y - 2(u_xQ + u_yS)] = -Q + 2au_x \tag{7a}$$

$$De[uS_x + vS_y - v_xQ - u_yR] = -S + a(u_y + v_x) \tag{7b}$$

$$De[uR_x + vR_y - 2(v_xS + v_yR)] = -R + 2av_y \tag{7c}$$

where subscripts denote partial differentiation. Here $a = 1/(Rv + 1)$ is the solute-to-solution viscosity ratio.

The above equations are solved subject to the no-slip and no-penetration boundary conditions

$$u(x, y=0) = v(x, y=0) = u(x, y=1+\varepsilon f(x)) = v(x, y=1+\varepsilon f(x)) = 0 \tag{8a}$$

and spatial periodicity

$$\phi(x=0, y) = \phi(x=\lambda, y), \quad p(x=0, y) = p(x=\lambda, y) - \lambda \Delta p \tag{8b}$$

where ϕ represents u, v, Q, R, or S, α is the dimensionless wavenumber of the wall modulation, and Δp is the linear pressure drop per unit length. Problems (6)–(8) is defined over the physical domain $\Omega_{xy} = \{(x, y) | x \in [0, \lambda], y \in [0, 1 + \varepsilon f(x)]\}$, as depicted, schematically, in Figure 1. This domain is next mapped onto the rectangular domain.

2.2. Domain transformation

The periodic physical domain Ω_{xy} is mapped onto the rectangular domain $\Omega_{\xi\eta} = \{(\xi, \eta) | \xi \in [0, \lambda], \eta \in [0, 1]\}$. In this case,

$$\xi(x, y) = x, \quad \eta(x, y) = \frac{y}{h(x)} \tag{9}$$

where $h(x) = 1 + \varepsilon f(x)$ is the dimensionless gap. Now the transformed equations read

$$u_\xi - u_\eta \eta \frac{h'}{h} + \frac{v_\eta}{h} = 0 \tag{10a}$$

$$Re\left[u\left(u_\xi - \frac{\eta h'}{h} u_\eta\right) + \frac{v u_\eta}{h}\right] = -\left(p_\xi - \frac{\eta h'}{h} p_\eta\right) + aRv\left[u_{\xi\xi} - 2\frac{\eta h'}{h} u_{\xi\eta} + \eta\left(\frac{h'}{h}\right)^2 (\eta u_{\eta\eta} + 2u_\eta) - \frac{\eta h''}{h} u_\eta + \frac{u_{\eta\eta}}{h^2}\right] + Q_\xi - \frac{\eta h'}{h} Q_\eta + \frac{S_\eta}{h} \tag{10b}$$

$$Re\left[u\left(v_\xi - \frac{\eta h'}{h} v_\eta\right) + \frac{v v_\eta}{h}\right] = -\frac{p_\eta}{h} + aRv\left[v_{\xi\xi} - 2\frac{\eta h'}{h} v_{\xi\eta} + \eta\left(\frac{h'}{h}\right)^2 (\eta v_{\eta\eta} + 2v_\eta) - \frac{\eta h''}{h} v_\eta + \frac{v_{\eta\eta}}{h^2}\right] + S_\xi - \frac{\eta h'}{h} S_\eta + \frac{R_\eta}{h} \tag{10c}$$

$$De\left[u\left(Q_\xi - \frac{\eta h'}{h}Q_\eta\right) + \frac{vQ_\eta}{h} - 2Q\left(u_\xi - \frac{\eta h'}{h}u_\eta\right) - \frac{2Su_\eta}{h}\right]$$
$$= -Q + 2a\left(u_\xi - \frac{\eta h'}{h}u_\eta\right) \tag{10d}$$

$$De\left[u\left(S_\xi - \frac{\eta h'}{h}S_\eta\right) + \frac{vS_\eta}{h} - Q\left(v_\xi - \frac{\eta h'}{h}v_\eta\right) - \frac{Ru_\eta}{h}\right]$$
$$= -S + a\left(v_\xi - \frac{\eta h'}{h}v_\eta + \frac{u_\eta}{h}\right) \tag{10e}$$

$$De\left[u\left(R_\xi - \frac{\eta h'}{h}R_\eta\right) + \frac{vR_\eta}{h} - 2S\left(v_\xi - \frac{\eta h'}{h}v_\eta\right) - \frac{2Rv_\eta}{h}\right]$$
$$= -R + 2a\frac{v_\eta}{h} \tag{10f}$$

where a prime denotes total differentiation. The boundary conditions become

$$u(\xi, \eta = 0) = u(\xi, \eta = 1) = v(\xi, \eta = 0) = v(\xi, \eta = 1) = 0 \tag{11a}$$

$$\phi(\xi = 0, \eta) = \phi(\xi = \lambda, \eta), \quad p(\xi = 0, \eta) = p(\xi = \lambda, \eta) - \lambda\Delta p \tag{11b}$$

where ϕ represents u, v, Q, R, or S.

The solution of the non-linear problem (10) is sought subject to condition (11). Despite the difficulty of the problem emerging from the additional viscoelastic terms and the non-linearity, the solution can be sought for some limit flows that are of practical and fundamental significance.

2.3. The perturbation solution

In this work, only small amplitude modulation is examined, so that ε is small ($\varepsilon \ll 1$). In this case, a regular perturbation expansion is used for the velocity, pressure, and the extra stresses. The regular perturbation expansion for any variable, ϕ, may be written as

$$\phi = \phi^{(0)} + \varepsilon\phi^{(1)} + \varepsilon^2\phi^{(2)} + O(\varepsilon^3) \tag{12}$$

where terms of $O(\varepsilon^3)$ and higher are neglected, and the superscripts $\phi^{(0)}$, $\phi^{(1)}$, and $\phi^{(2)}$ represent the leading, first, and second-order perturbation parameters. Substitution of expression (12) into Equations (10) and conditions (11) leads to a hierarchy of equations and boundary condition that must be solved to each order in ε. Thus, to leading order in ε, one recovers the equations encountered in conventional Poiseuille flow. Correspondingly the solution is given by

$$\begin{aligned} u^0 &= 4\eta(1-\eta), \quad v^0 = 0, \quad p^0_\xi = -8 \\ Q^0 &= 2aDeu^{0^2}_\eta, \quad R^0 = 0, \quad S^0 = au^0_\eta \end{aligned} \tag{13}$$

where the subscripts donate partial differentiation, and superscript brackets have been dropped for simplicity. The equations and the boundary conditions to $O(\varepsilon)$ and $O(\varepsilon^2)$ are detailed in Appendix A in Reference [48].

At this point, it is necessary to introduce explicitly the modulated wall profile, f. Various configurations may be easily incorporated in the general formulation above. For instance, both walls could be assumed to be modulated, and the modulation can be represented by a general Fourier series, as long as the wall profile is smooth. In this work, however, only the upper wall is assumed to be modulated in the form of a sine wave such that

$$f(\xi) = -\cos(\alpha\xi) \tag{14}$$

where α is recalled to be the dimensionless wavenumber. Because of the periodicity of the flow, the general solution to any of the perturbated variables ϕ, may be expressed in terms of Fourier series, such as

$$\phi(\xi,\eta) = \phi^0(\xi,\eta) + \varepsilon \sum_{n=1}^{\infty} \phi_n^{11}(\eta)\sin(n\alpha\xi) + \phi_n^{12}(\eta)\cos(n\alpha\xi)$$

$$+\varepsilon^2 \sum_{n=1}^{\infty} \phi_n^{21}(\eta)\sin(n\alpha\xi) + \phi_n^{22}(\eta)\cos(n\alpha\xi) + O(\varepsilon^3) \tag{15}$$

where terms of $O(\varepsilon^3)$ and higher are neglected. Substitution of expressions (15) into Equations (11) and conditions (12), lead to a system of non-homogeneous differential equations for the perturbated coefficients, constituting a boundary-value problem of the two-point type. These equations and boundary conditions are given in Appendix B in Reference [48]. The solution is obtained through a variable-step finite-difference scheme (IMSL-DBVPFD) with a tolerance equal to 10^{-6}. The basic discretization is the trapezoidal rule over a non-uniform mesh. This mesh is chosen adaptively, to make the local error approximately the same size everywhere. Higher-order discretizations are obtained by differed corrections and global error estimates are produced to control the computation. The linear system of equations is solved using a special form of Gauss elimination that preserves sparseness.

3. NUMERICAL ASSESSMENT

The perturbation approach is intended to provide a fast and accurate alternative to conventional numerical methods in the limit of small modulation amplitude. Since the dependence of the solution in the axial direction is expressed analytically for the domain perturbation analysis, unlike finite element or finite volume methods the convergence rate and storage requirements for the perturbation analysis are not an issue. In fact, the domain perturbation analysis is an order of magnitude faster than the finite element or the finite volume method [14, 27]. It is thus important to establish its accuracy and range of validity for viscoelastic flow. For Newtonian fluid, Zhou *et al.* [13, 14] showed that first-order perturbation approach predicts the velocity and pressure fields accurately (within 1%) for $\varepsilon \leqslant 0.2$ and $\alpha \leqslant 5$. Whether elastic effects reduce the geometric validity range for the perturbation approach is still an unanswered question.

Error sources for the perturbation method are in the truncated terms. These terms contain combinations of the velocity gradients multiplied by coefficients containing the parameters α, ε, Re, De, and Rv. The influence of the truncated terms on the continuity equation is conveniently summarized through the global error in mass conservation, since only the mean pressure gradient is imposed in the solution procedure. Letting Q_{ave} be the average over one modulation period of the flow rate Q at each x location, the maximum relative error may then be defined as

$$\Delta = \frac{|Q - Q_{\text{ave}}|_{\max}}{Q_{\text{ave}}} \tag{16}$$

The influence of the modulation amplitude on the maximum error is shown in Figure 2, where Δ is plotted against ε for $\alpha = 1$, $Re = 0$, $De = 4$, $Rv = 1$. As expected, for the first-order perturbation analysis the error is on the order of ε^2, and conservation of mass is generally satisfied to within 1% for $\varepsilon < 0.15$. The error is reduced to become on the order of ε^3 for the second-order perturbation solution, and conservation of mass is generally satisfied to within 1% for $\varepsilon < 0.28$. Additional calculations were carried out for several values of α, Re, De, and Rv. The influence of the wavenumber, inertia, and viscoelastic effects on the overall error appears to be negligible when $\varepsilon < 0.28$ when second-order perturbation terms are included. This was confirmed through calculations for $0.1 < \alpha < 2\pi$ and $0 < Re < 6000$ and for $Rv \in [0, \infty)$ and $De \in [0, 12]$. The only influencing parameter appears to be the modulation amplitude, ε.

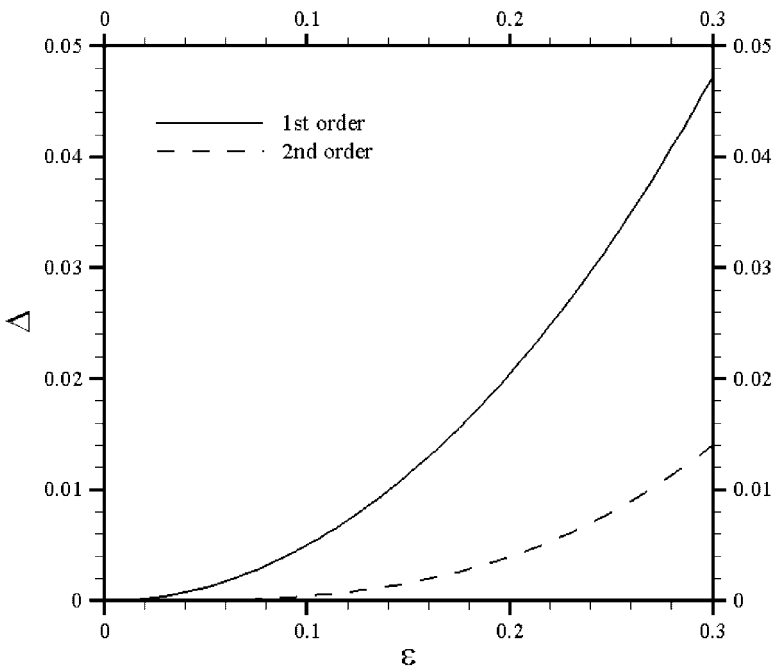

Figure 2. Maximum relative error for mass conservation as functions of the modulation amplitude, ε. Note that the curves are essentially independent of the remaining parameters.

Comparison with experimental results provides an extra source for accuracy assessment. However, reliable experimental results for steady-state Oldroyd-B fluid flow through channels of arbitrary shapes are unattainable. Yalamanchili *et al.* [10, 11] experimental results cannot be used for comparison because of two reasons. First, Although the examined dilute polymeric solution (polyacrylamide) can be described using the Oldroyd-B constitutive equation [47, 49, 50], incomplete information about the fluid properties prevent an accurate comparison with any numerical results. Yalamanchili *et al.* did not report the type of the polyacrylamide used in their experiment. Further examination of Yalamanchili's findings discloses some conflicting results. For example, while Figure 7 in Reference [10] shows the centreline velocity for a mixture of 60% water and 40% glycerin to fluctuate around $10 \pm 0.5\,\mathrm{cm/s}$ at $Re = 70.5$, the centreline velocity is reduced to $3 \pm 0.2\,\mathrm{cm/s}$ for the same fluid at the same Reynolds number in the same channel in Figure 10 in Reference [10].

Although direct comparison with reliable experimental results for a viscoelastic flow is unachievable, perturbation approach seems to be reasonably accurate in predicating the flow kinematics and stress fields for both Newtonian and non-Newtonian fluids. In particular, Abu-Ramadan and Khayat [45] compared the shear induced flow fields inside periodically modulated channels assessed by the perturbation approach to that evaluated using a finite-volume code, FLUENT, for shear-thinning fluids. They show that the first-order perturbation solution is accurate to within ε^2. Thus, they establish that non-Newtonian's parameters do not affect the validity range of the perturbation approach. Furthermore, Sureshkumar [27] showed that for purely elastic steady flow, the maximum flow resistance difference between the second-order domain perturbation analysis and the more accurate finite element approach is less than 3% for dimensionless wall amplitude, wavenumber and De equal to 0.15, 1, and 4.5, respectively.

The validity of the applied second-order perturbation approach can be quantitatively assessed in the Newtonian limit, where numerous experimental and numerical studies have been preformed. Although Zhou *et al.* [13, 14] have established the accuracy of the perturbation approach through comparison with the finite volume approach; direct comparison with experimental results was not reported. The most reliable experimental investigation for Newtonian flow has been carried out by Hudson *et al.* [51]. They used Laser Doppler velocimetry to measure spatial and time variation of the two-dimensional flow field through a channel with sinusoidal bottom wall and a flat top wall. Günther and von Rohr [15] confirmed the vortex size and location using particle image velocimetry (PIV). Figure 3 compares Hudson *et al.* experimental results (left) with the second-order domain perturbation method results (right) for $Re = 10\,050$, $\varepsilon = 0.05$, and $\alpha = 2\pi$. This figure shows the mean velocity field (arrows) and the streamlines. Although the reported Reynolds number is larger than the critical Reynolds number for onset of instability in non-modulated (Poiseuille) channel flow, the reported flow presents the time-average flow field. Qualitatively, both techniques, experimental and numerical, predict similar flow fields. A separated region or a vortex appears in the diverging section of the channel near the modulated wall. A region of large velocity gradients close to the modulated wall appears downstream of the vortex. Quantitative differences between experimental and numerical results exist. Experimental results show that the vortex extends between $x/\lambda = 0.3$ and $x/\lambda = 0.5$. Second-order perturbation method seems to overestimate the vortex size, which extends between $x/\lambda = 0.18$ and 0.7. Neglecting second-order perturbation terms leads to even much larger vortex size. A valid explanation for the quantitative deviation can be related to the difficulties reported in obtaining experimental results for small wall

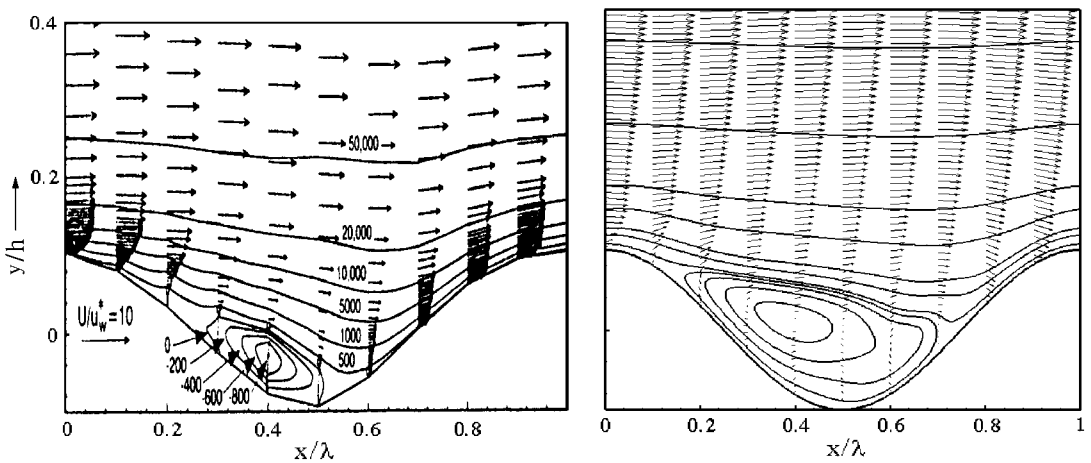

Figure 3. Comparison between Hudson *et al.* [51] experimental results (left) and the current study perturbation method results (right) for Newtonian fluid. Here $Re = 10050$, $\varepsilon = 0.05$, and $\alpha = 2\pi$.

modulation ($\varepsilon < 0.2$) [1, 31–34]. From the experimental vortex structure in Figure 3, those difficulties are not surprising. In the small amplitude range, the separation point occurs far downstream of the cusp at the wall trough and is susceptible to upstream perturbations.

Since the domain perturbation approach is CPU efficient, and it can produce faithfully accurate results for weakly modulated channels [2, 4, 13, 14, 27], it will be implemented here to investigate the flow characteristics and vortex formation for pressure driven Oldroyd-B fluid type flow through weakly modulated channels. It has been shown that second-order perturbation approach [27] generates more accurate results than the first-order perturbation approach with hardly any extra CPU and storage capacity. Furthermore, the first non-zero correction to the flow resistance as compared to the Poiseuille flow occurs at the second order [2]. Hence, it is important to account for those terms throughout this study. All the presented results throughout this section are obtained through the second-order perturbation analysis.

4. DISCUSSION AND RESULTS

In this section, viscoelastic flow inside a weakly modulated channel will be considered. To establish separate effect of elasticity on the flow kinematics and stress distributions, purely elastic flow will be examined first. The influence of inertia will be assessed afterwards. The interplay between elastic and inertia effects will also be addressed. Since geometric parameters can alter the critical conditions for the onset of backflow for Newtonian fluid [1, 12–14, 32, 35, 37], their influence on the vortex size, measured by the distance between the separation and reattachment points, and vortex location, especially near the lower wall, will be examined for viscoelastic fluids.

4.1. Purely elastic flow

Consider purely elastic flow ($Re = 0$) with $Rv = 1$, $\varepsilon = 0.1$ and $\alpha = 1$. The general flow response is typically illustrated in Figure 4 for a flow inside a modulated channel with $De = 4$. The figure shows the streamlines, the contours of pressure departure (from linear pressure), p^e, velocity components in the streamwise, u, and depthwise, v, directions, the shear stress, τ_{xy}, and the normal stress difference, $N = \tau_{xx} - \tau_{yy}$. The figure shows a comparison between the streamlines obtained for creeping Newtonian flow (dashed lines) and purely elastic flow (solid lines). Although the streamlines for both creeping Newtonian and purely elastic flows follow generally the channel wall profile, elasticity tends to cause a slight distortion in the symmetry of the flow field with respect to the channel crest. The loss of symmetry amplifies upon increasing De or decreasing Rv. The distortion in the flow field is attributed to presence of the upper-convective terms in the constitutive equations, and the ensuing normal stress effect. Investigating the influence of elasticity on the pressure and stress fields is, thus, essential.

Figure 4 indicates that while the pressure departure varies little across the channel, a break in symmetry with respect to the crest location is clearly depicted. Pressure variation across the channel is more obvious downstream of the crest and trough locations, where the pressure is maximum and minimum, respectively. The influence of elasticity on the flow kinematics is inferred from the velocity contours in the streamwise and depthwise directions, which confirm the break in symmetry. Inspection of the u and v contours show that the depthwise flow is much weaker than the streamwise flow, on the order of 5%. It is also inferred that the changes in v with respect to both x and y are smaller than the change in u with respect to y. Moreover, u is not expected, given the weak modulation amplitude, to change rapidly with x.

The deviation of the viscoelastic flow from the Newtonian flow is best reflected by the stress distribution across the channel. The contours of τ_{xy} and N for creeping Newtonian flow are examined first as reported by Davidson *et al.* (see Figure 1 in Reference [19]). It is found that creeping Newtonian flow through periodically modulated geometries is characterized by a symmetric shear stress, τ_{xy}, distribution about the crest [2, 14, 19]. The maximum shear stress amplitude occurs at the trough of the modulated wall along which τ_{xy} is negative. There is a change in sign from negative at the upper section of the channel to positive at the lower section of the channel along the centre plane. Comparison between the viscoelastic stress distribution in Figure 4 and the Newtonian stress distribution indicates that while elasticity dramatically alters the τ_{xy} distribution near the upper modulated wall, it has hardly any effect along the centre plane where τ_{xy} is negligibly small. Little effect is observed near the lower wall. In addition, steep boundary layers are predicted in the region next to the modulated wall.

Creeping Newtonian flow through periodically modulated channel is characterized by an anti-symmetric N distribution about the crest [2, 14, 19]. Near the modulated wall, N is positive in the converging section of the channel, and changes its sign at the crest. Figure 4 shows that for a purely elastic flow N is positive everywhere across the channel and sharp stress gradients occur near the walls. These gradients develop near the walls as elasticity is introduced, confirming the earlier results of Pilitsis and Beris [2]. As expected, elasticity results in a vast increase in N. In particular, it is found that the maximum N increases from 1.46 to 85 as De increases from 0 to 4 for the set of geometric parameters used in Figure 4.

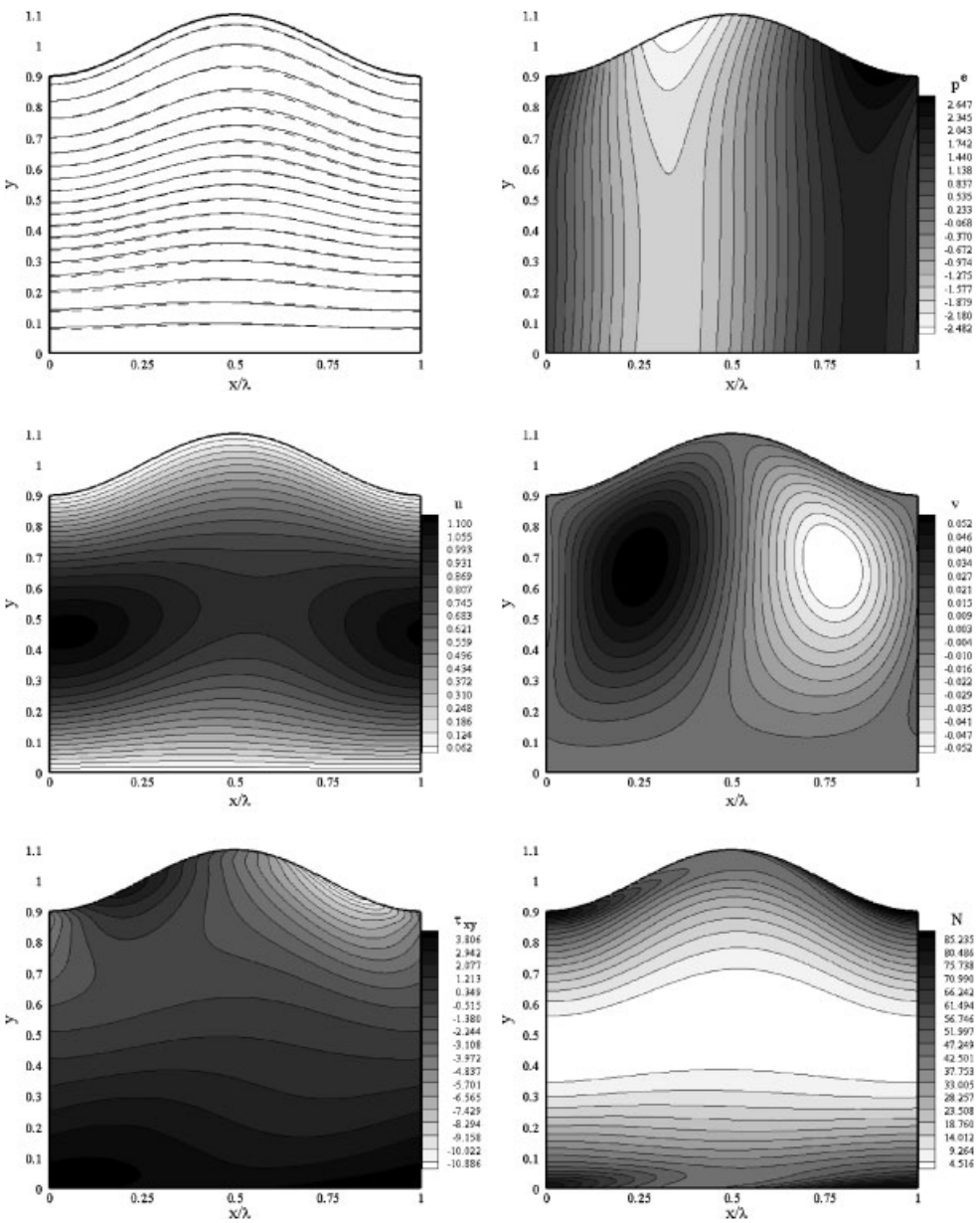

Figure 4. Typical response of purely elastic flow ($Re = 0$). The figure displays the streamlines, the pressure departure, p^e, the contours of the streamwise and depthwise velocity components, u and v, shear stress distribution, τ_{xy}, and normal stress difference, N. Here $\varepsilon = 0.1$, $\alpha = 1$, $Rv = 1$, $De = 4$. The solid streamlines present viscoelastic flow and the dashed lines are for Newtonian flow ($De = 0$).

The quantitative deviation from the Newtonian limit is investigated upon examining the pressure profiles along the walls for various De as shown in Figure 5. The creeping Newtonian flow is characterized by a sinusoidal anti-symmetric pressure distribution along the walls. Viscoelastic pressure profiles display a gradual deviation from sinusoidal behaviour as elasticity increases, with elasticity causing a downstream shift of the location of the extrema. As elasticity increases, the extrema are shifted further downstream, as indicated by the loci of the extrema in Figure 5. The shift in the extrema location contributes to the distortion in the flow field as indicated by Figure 4 (see above). Furthermore, elasticity influences the pressure in a non-monotonic manner. Figure 5 shows that for low values of elasticity, $De<4$, the amplitude of the pressure departure for a viscoelastic fluid is lower than that for a Newtonian fluid. Once De exceeds a critical value, De_{crt} (in this case ≈ 5), $|p^e|$ increases with elasticity. Similar behaviour has also been observed experimentally by Rothestein and McKinely [18] for viscoelastic flow through a 4:1:4 axisymmetric contraction/expansion duct. They showed that De_{crt} is close to the Deborah number at which coil-stretch transition occurs in a homogenous extensional flow. For $De>0$, one can infer from both Figures 4 and 5 that pressure experiences a steeper change near the extrema at the upper wall than at the lower wall. The extrema occur at the same x locations at the two walls, but $|p^e|$ is slightly stronger at the upper wall. Pilitsis and Beris [2] suggested that pressure rather than viscoelastic stresses dominate forces developed normal to the streamlines as elasticity increases. In other words, Pilitsis and Beris [2] suggested that stresses have little effect on the forces normal to the streamlines. This suggestion is confirmed by the comparison of the pressure and normal forces profiles along the walls, regardless of the De level, at both the lower and upper walls.

The effect of elasticity for creeping flow is further assessed by examining the normal stress distribution in Figure 6, which shows the N profiles at the upper and lower walls for $0\leqslant De\leqslant 10$. Elasticity causes a break in the sinusoidal Newtonian normal stress distribution along the upper wall. As De increases from 0 to 2, the maximum and the minimum N relocate from $x/\lambda=0.25$ and 0.75, respectively, to 0.95 and 0.5. Further increase in De results in an upstream shift of the extrema locations. The figure indicates that normal stress amplitude increases almost linearly with De, similarly to straight Poiseuille flow. Furthermore, viscoelastic N profiles near the upper wall is almost identical to its profiles near the lower wall. This identical behaviour is absent for Newtonian fluid. While N is sinusoidally distributed near the upper modulated wall, it is zero near the lower wall for Newtonian fluid. The domination of the extra stresses developed in viscoelastic fluids over the normal stresses developed due to extensional character of the modulation can explain the vast difference between viscoelastic and Newtonian normal stress distribution and amplitude.

The effect of elasticity is quantified further upon inspection of τ_{xy} profiles near the walls. Figure 7 shows that at the modulated wall, elasticity changes the shear stress distribution. For Newtonian flow, τ_{xy} is always negative, and the fluid is subject to higher shear stress in the narrow cross section. For viscoelastic flow, τ_{xy} shows a maximum in the diverging section of the channel and a minimum in the converging section of the channel. In agreement with earlier results [2, 6, 7, 19], the shear stress is more concentrated in the converging section of the channel. In particular, the amplitude of τ_{xy} in the converging section of the channel is almost double its amplitude in the diverging section. This is due to the elastic stress buildup in the converging region. Furthermore, the shear stress amplitude increases almost linearly as a function of elasticity. This is in agreement with earlier results by numerous investigators [2, 6, 7]. This behaviour is due to the additional stresses resulting from the constitutive

equation (2), which is characterized by a solid-like behaviour at high values of elasticity [6]. Investigating the influence of elasticity on τ_{xy} distribution along the lower wall reveals distinctly different qualitative behaviour in comparison with τ_{xy} profile at the upper wall. First, while the location of τ_{xy} extrema is hardly altered by elasticity at the upper wall, the extrema are shifted upstream at the lower wall as elasticity increases. Second, τ_{xy} amplitude decreases as elasticity increases at the lower wall. In particular, as *De* increases from 0 to 2, τ_{xy} amplitude doubles at the upper wall and decreases by around 4% at the lower wall. The relative insignificant influence of elasticity on shear stress along the lower wall can be understood from the definition of τ_{xy}, which is expressed as

$$\tau_{xy} = aRv(u_y + v_x) + S \tag{17}$$

At the lower wall, $S = au_y$ as indicated by Equation (7), with $v_x = 0$. Thus, τ_{xy} is reduced to u_y at the lower wall. Since it has been illustrated earlier that elasticity has relatively small effect on the flow kinematics at the lower wall (see above), τ_{xy} profiles near the lower wall will be slightly affected by elasticity. The slight break in symmetry in the viscoelastic velocity contours (see Figure 4) is reflected in τ_{xy} profiles near the lower wall.

The correlation between elastic effect on the flow kinematics and shear stress is inferred from Figures 7 and 8. Figure 8 shows the vorticity ζ, $\zeta = v_x - u_y$, distribution along the upper and lower walls for various *De*. Note that, at the lower wall, $\tau_{xy} = -\zeta$. Although elasticity causes a symmetry breaking in the ζ distribution, with respect to the crest along the walls, it results in a smoother variation of ζ along the walls. An increase in *De* results in an upstream shift and reduction in the values of the extrema. Thus, elasticity tends to minimize the effect of the modulation, making the creeping flow behave similarly to that between two flat plates.

Comparison between creeping Newtonian and purely elastic flows shows that elasticity alters stress and pressure distributions with minimal effect on the flow kinematics. Although this observation confirms earlier numerical results obtained by Pilitsis and Beris [2] and Davidson *et al.* [19], it contradicts the experimental findings of Davidson *et al.* [19], who reported that non-Newtonian effects are first observed in the flow kinematics and not in the stresses. This contradiction is apparently attributed to the inadequacy of the constitutive model used in their finite-element calculations. Both the UCM and White-Metzner model were used. The insignificant change in flow kinematics resulting from elasticity is clearly due to the little change in pressure gradient as *De* increases as shown in Figure 5. The results above show that elastic effects are more noticeable near the modulated wall. However, this conclusion is limited to purely elastic fluids.

4.2. Influence of inertia for viscoelastic flow

It is well established, for Newtonian flow, that as the Reynolds number exceeds a certain threshold, flow separation occurs in the region of expansion (below the crest). In this case, the threshold depends on the modulation amplitude and wavelength. A similar response is expected for a viscoelastic fluid, but fluid elasticity is expected to influence the conditions for the onset of separation. The general flow response for a viscoelastic fluid that exhibits backflow is typically illustrated in Figure 9. Here $\varepsilon = 0.1$, $\alpha = 1$, $De = 4$, $Rv = 1$, and $Re = 2500$. The overall effect of inertia is observed by comparing the current flow to that in Figure 4 for $Re = 0$, the remaining parameters being the same. These two flows are typical of the pre- and

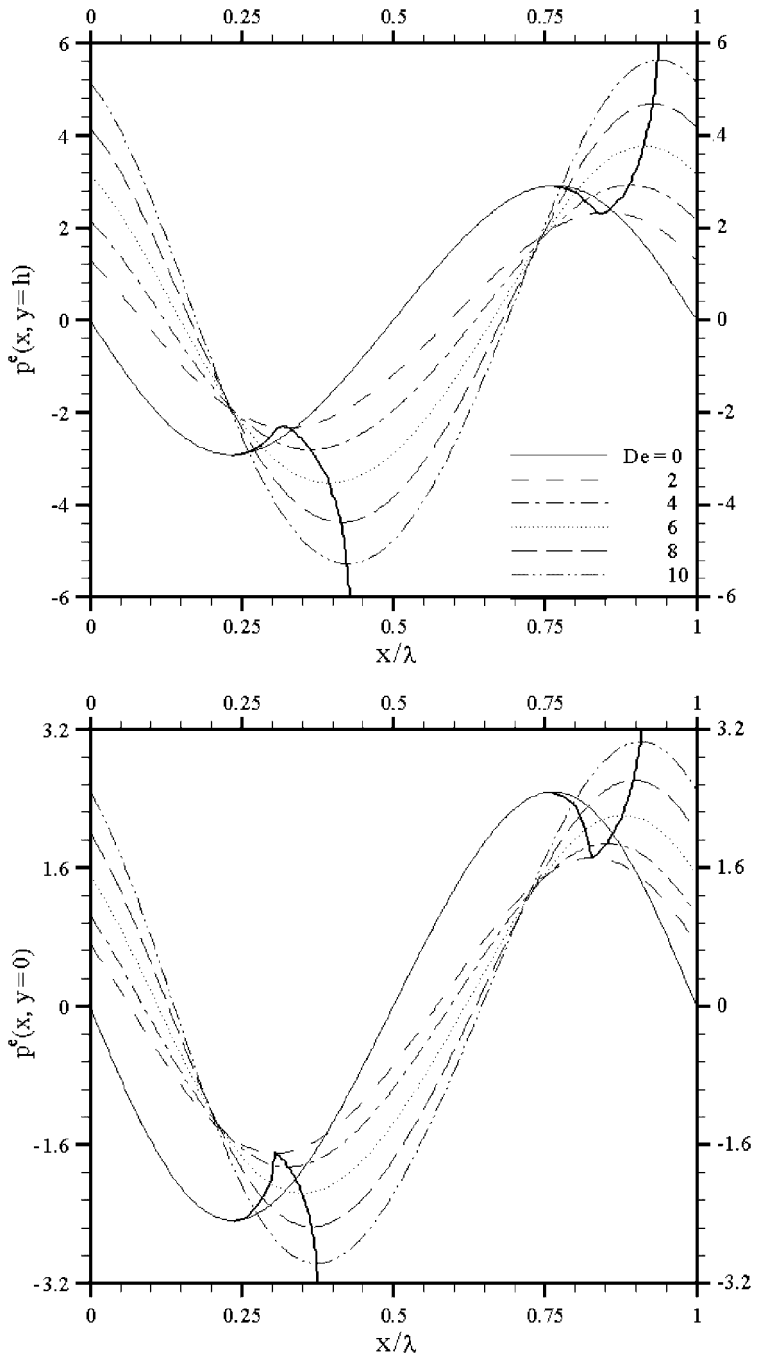

Figure 5. Elastic effects on the pressure departure profiles, p^e, along the upper and lower walls for purely elastic fluid. Here $Rv = 1$, $\varepsilon = 0.1$, and $\alpha = 1$.

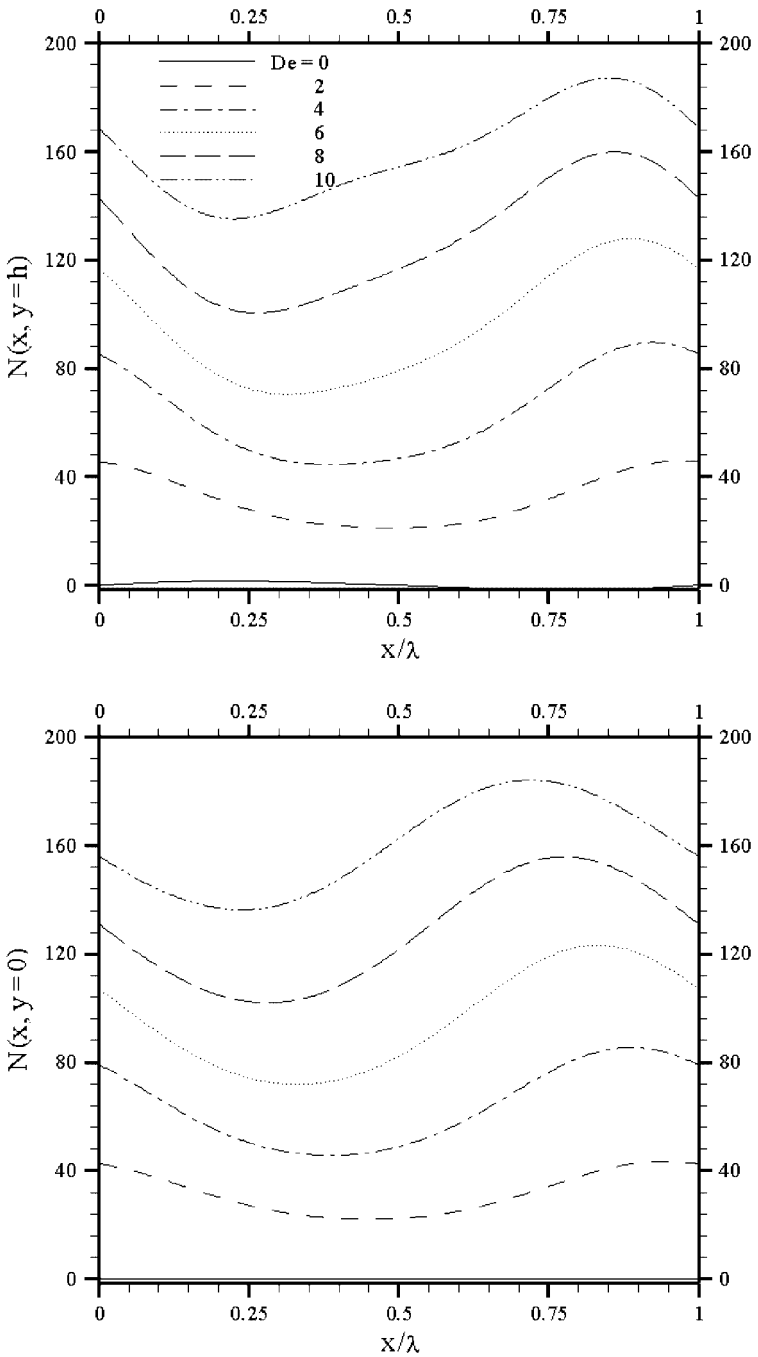

Figure 6. Elastic effects on the normal stress difference distribution, N, along the upper and lower walls for purely elastic fluid. Here $Rv = 1$, $\varepsilon = 0.1$, and $\alpha = 1$.

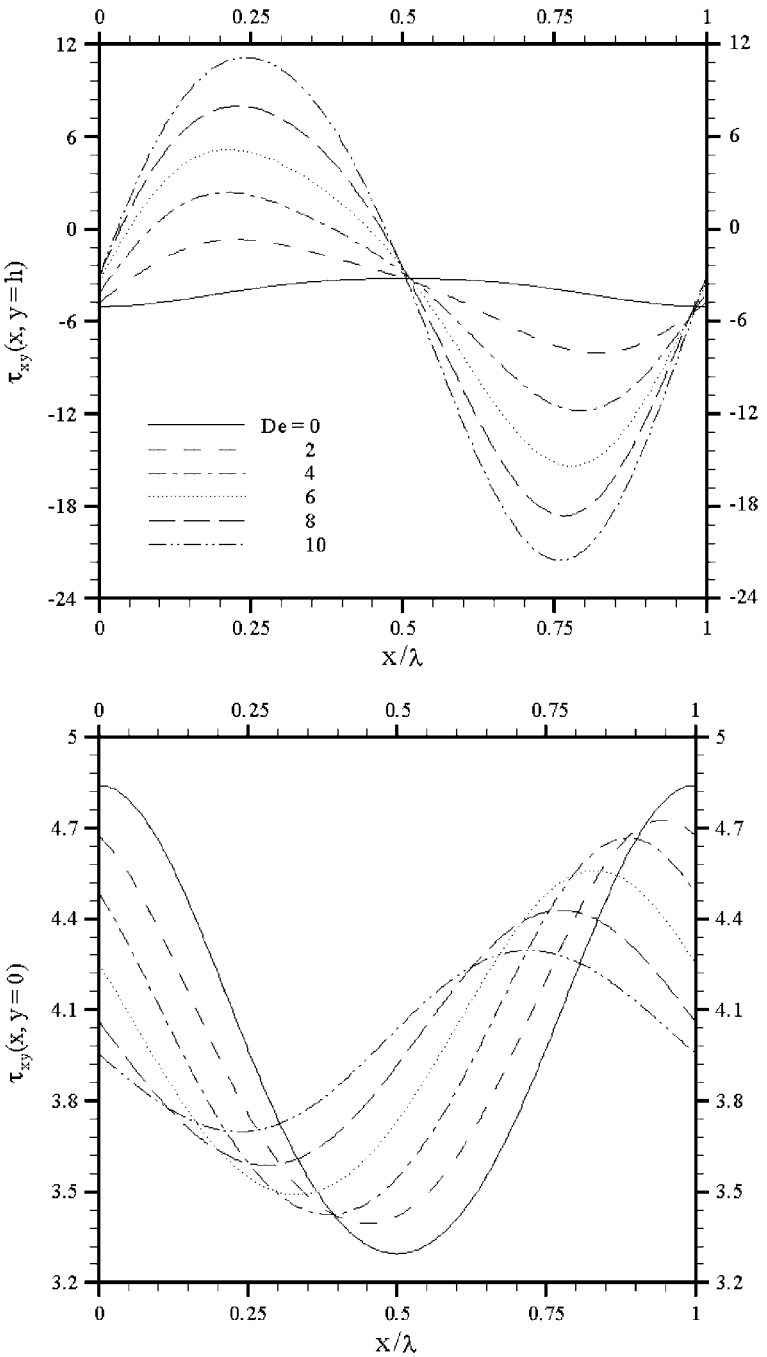

Figure 7. Elastic effects on the shear stress distribution, τ_{xy}, along the upper and lower walls for purely elastic fluid. Here $Rv = 1$, $\varepsilon = 0.1$, and $\alpha = 1$.

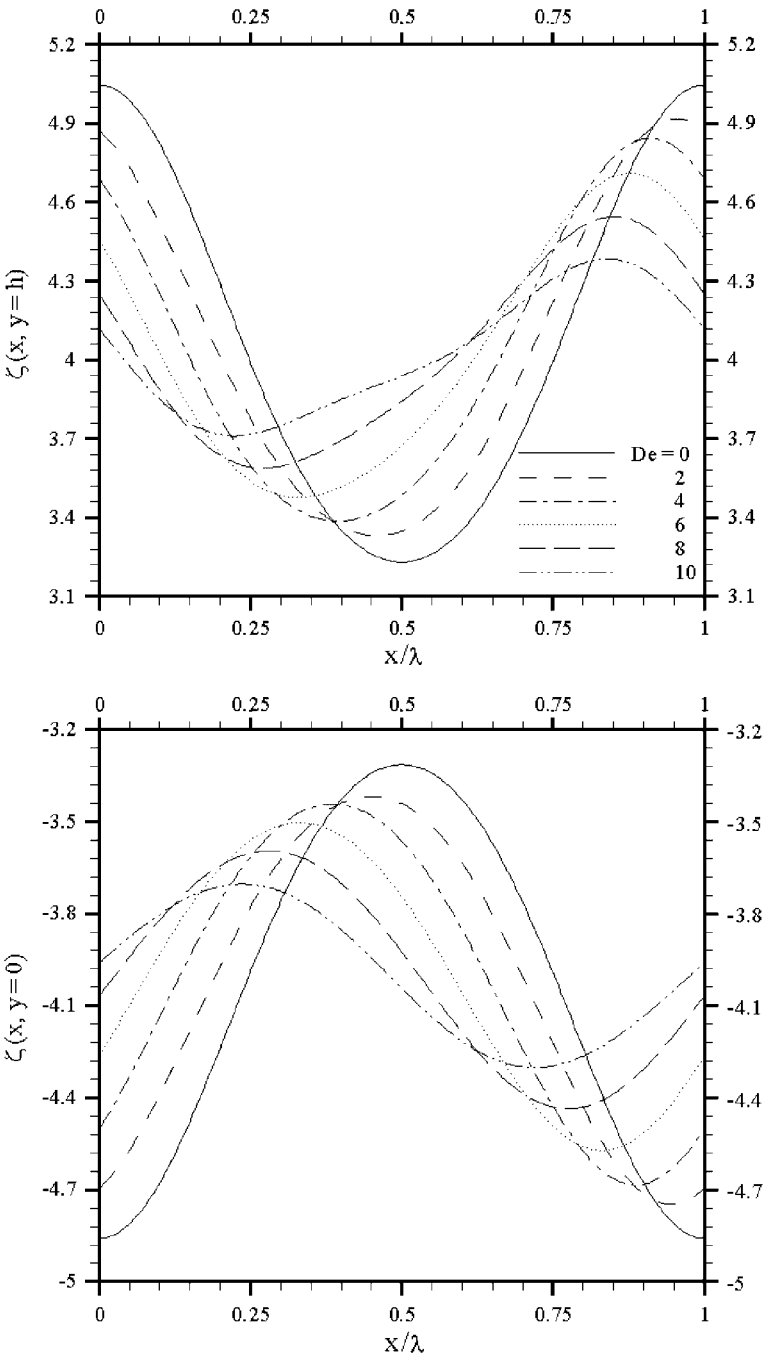

Figure 8. Elastic effects on vorticity distribution, ζ, along the upper and lower walls for purely elastic fluid. Here $Rv = 1$, $\varepsilon = 0.1$, and $\alpha = 1$.

the post-critical ranges of Reynolds number. As will be discussed later, the critical Reynolds number at which the flow separates is strongly influenced by fluid and geometry parameters.

A significant difference in streamline topology between Figures 9 and 4 is the appearance of a backflow region below the crest. The flow reattaches immediately downstream of the crest resulting in a significant loss of symmetry. Comparing p^e contours from Figures 9 and 4 shows that inertia causes an upstream shift in the location of pressure extrema. The pressure exhibits a minimum below the trough and a maximum downstream of the crest. The depthwise pressure variation across the channel is more pronounced when inertia is present. More importantly, the pressure magnitude increases significantly as inertia increases. The magnitude of p^e increases 40 times as Re increases from 0 to 2500. Thus, a positive correlation between pressure gradient and inertia occurs. A large pressure gradient would force separation to occur, which is consistent with the present result. The appearance of the backflow causes the core region of the flow to expand less into the cavity, resulting in a smaller depthwise velocity, v. The separation streamline reduces the effective cross-sectional flow area. Consequently, as a result of continuity the streamwise velocity in the channel core remains high and the streamlines outside the recirculation are no longer parallel to the wall and thus the maximum v is reduced when compared to the creeping case. The depthwise velocity contours exhibit a break in symmetry. The v contours are skewed downstream under the influence of inertia. Despite the apparent significance of the backflow, the magnitude of the velocity in the reverse direction is only 2% of the maximum in u (in the core region).

Inertia effect on the stress distribution for a viscoelastic fluid is inferred from the contours of shear stress, τ_{xy}, and normal stress difference, N. Comparison with Figure 4 shows that inertia results in increasing the magnitude of τ_{xy} and N near the upper and lower walls. In particular, inertia causes the maximum N to increase by 300% and the maximum τ_{xy} by 89%. This increase in magnitude is accompanied by sharper stress gradients near the upper wall for both N and τ_{xy}, and near the lower wall for N only. Stress distribution along the boundaries is dramatically altered by inertia. This point will be revisited later (see Figures 11 and 12). A correlation between shear stress profiles near the walls and the appearance of backflow does not appear to exist for viscoelastic fluids. It is worth mention that in addition to Zhou *et al.* [13, 14], Tsangaris and Leiter [32] demonstrated that for a Newtonian fluid, the switch in the τ_{xy} sign indicates the onset of backflow.

The influence of inertia is further investigated upon examining the pressure profiles at both the upper and lower walls for the range $Re \in [0, 3000]$ as shown in Figure 10. Inertia causes an upstream shift in the extrema locations (see the change from $Re = 0$ to $Re = 500$). Further increase in inertia results in an increase in the pressure magnitude with insignificant influence on the extrema locations. Pressure magnitude along the upper wall is higher, leading to a larger pressure gradient at the upper wall. Thus, backflow is more likely to occur first near the upper wall. More importantly, increasing inertia results in a monotonic increase in the pressure. The increase in the pressure magnitude is due to inertial non-linear effects regardless of whether a backflow appears or not [4, 12, 14, 37]. Both viscoelastic and Newtonian fluids exhibit similar pressure profiles in the inertial regime. In particular, elasticity has negligible effects on the pressure in the inertial regime. This behaviour is not surprising since Figure 5 shows that for creeping flow near the upper wall, as De increases from 0 to 4, the pressure is only slightly affected. Similar behaviour is expected to exist in the inertial regime. This is in agreement with earlier experimental investigation by James *et al.* [24], where elasticity was found to have little effect on the flow resistance in the inertial regime.

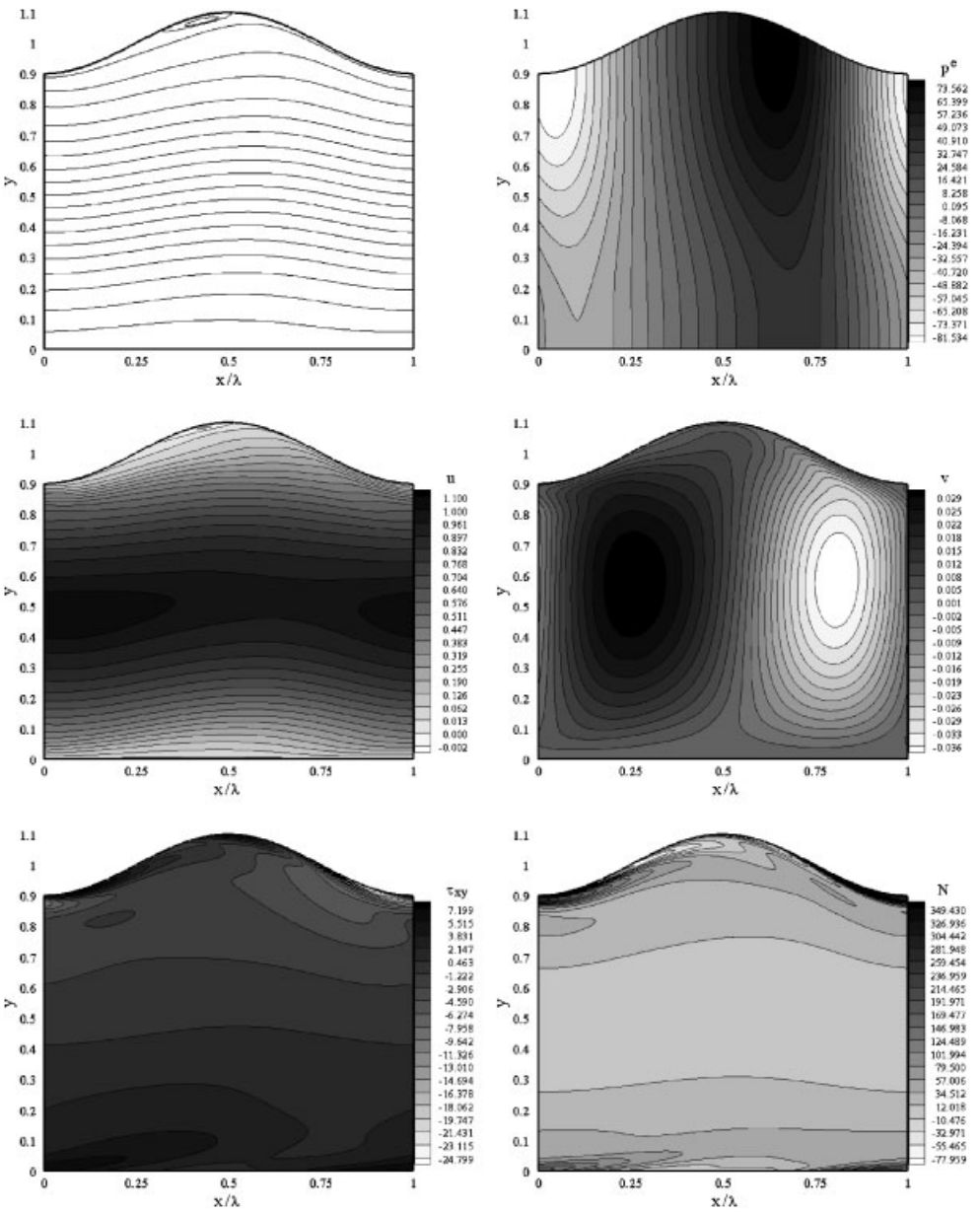

Figure 9. Typical response of viscoelastic flow with high inertia ($Re = 2500$). The figure displays the streamlines, the pressure departure, p^e, the contours of the streamwise and depthwise velocity components, u and v, shear stress distribution, τ_{xy}, and normal stress difference, N. Here $\varepsilon = 0.1$, $\alpha = 1$, $Rv = 1$, and $De = 4$.

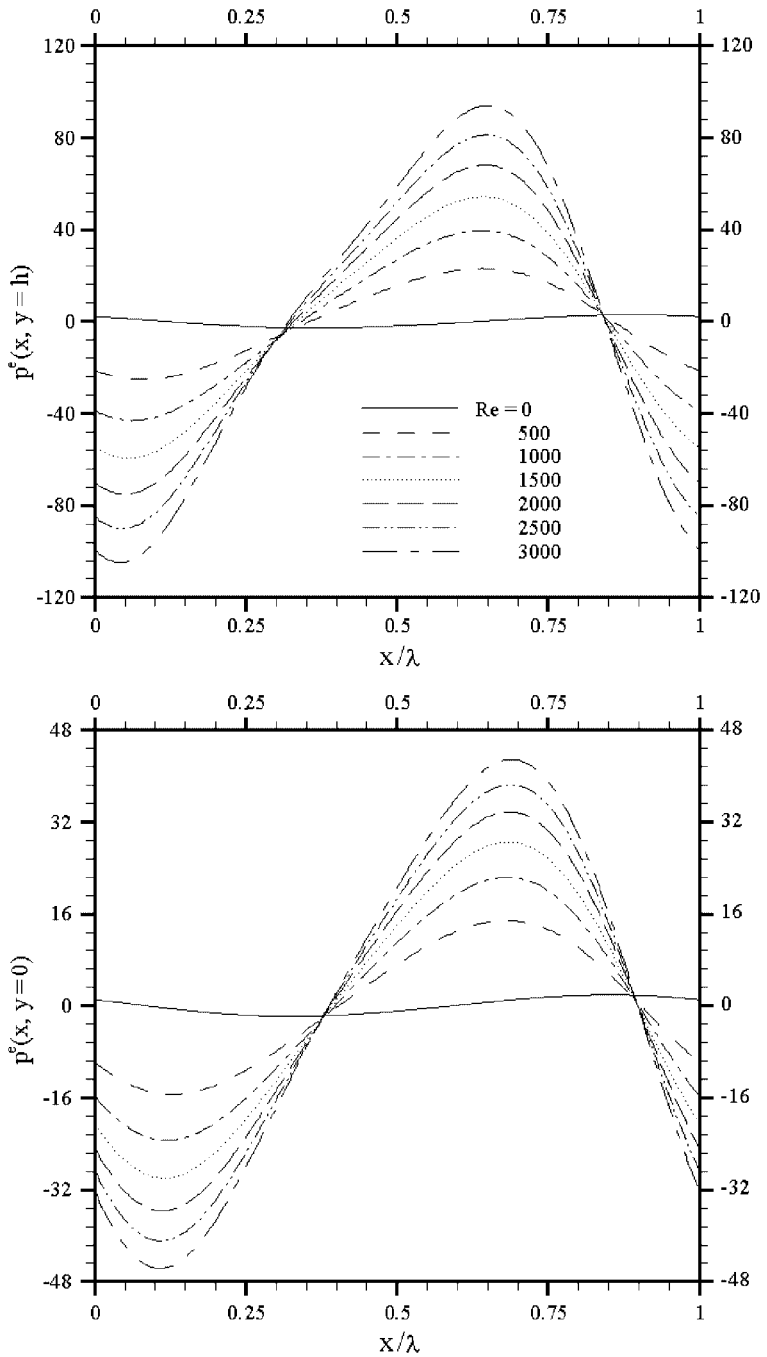

Figure 10. Inertia effects on the pressure departure, p^e, along the upper and lower walls for viscoelastic fluid ($De = 4$, and $Rv = 1$). Here $\varepsilon = 0.1$ and $\alpha = 1$.

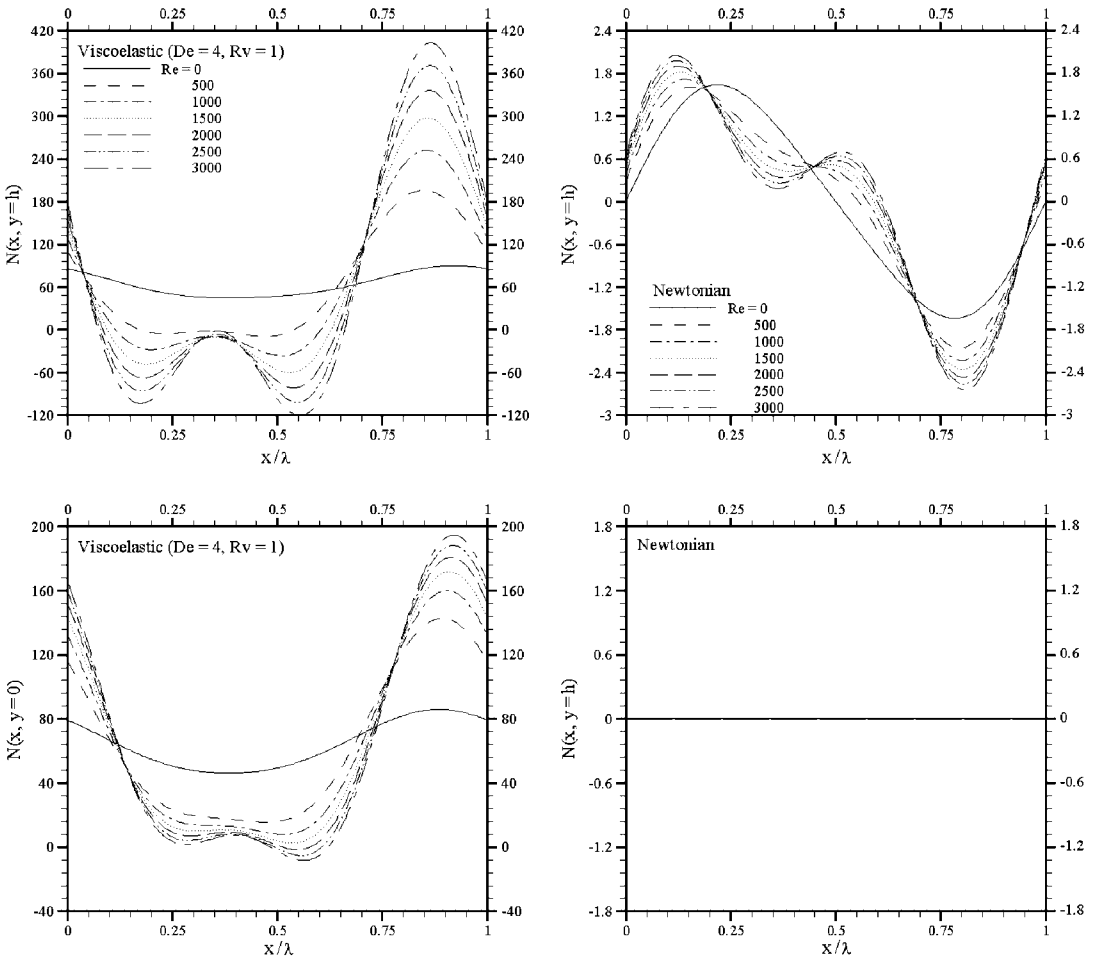

Figure 11. Inertia effects on the Normal stress difference distribution, N, along the upper and lower walls for viscoelastic fluid ($De = 4$, $Rv = 1$), left, and Newtonian fluid, right. Here $\varepsilon = 0.1$ and $\alpha = 1$.

Since most of the changes in the stress occur near the walls, investigating N and τ_{xy} distribution along the walls for various Reynolds numbers is important. Figure 11 shows N profiles at the upper and lower walls for a viscoelastic fluid ($De = 4$, $Rv = 1$), and Newtonian fluid for the range $Re \in [0, 3000]$. At the upper wall, increasing inertia results in a simultaneous increase in the magnitude of N for both fluids. Viscoelastic fluids are characterized by larger N in comparison with Newtonian fluid regardless of Re. Notice the appearance of several relative maxima for both fluids near the upper wall. The normal stress difference profiles in Figure 11 are closely related with the depthwise velocity contours in Figure 9. Close inspection of the velocity contours shows that inertia effects on the vertical velocity gradient along the upper wall, v_y, is behind the appearance of various relative extrema. Near the lower wall, while N for a Newtonian fluid is negligible near the lower wall, inertia affects the N

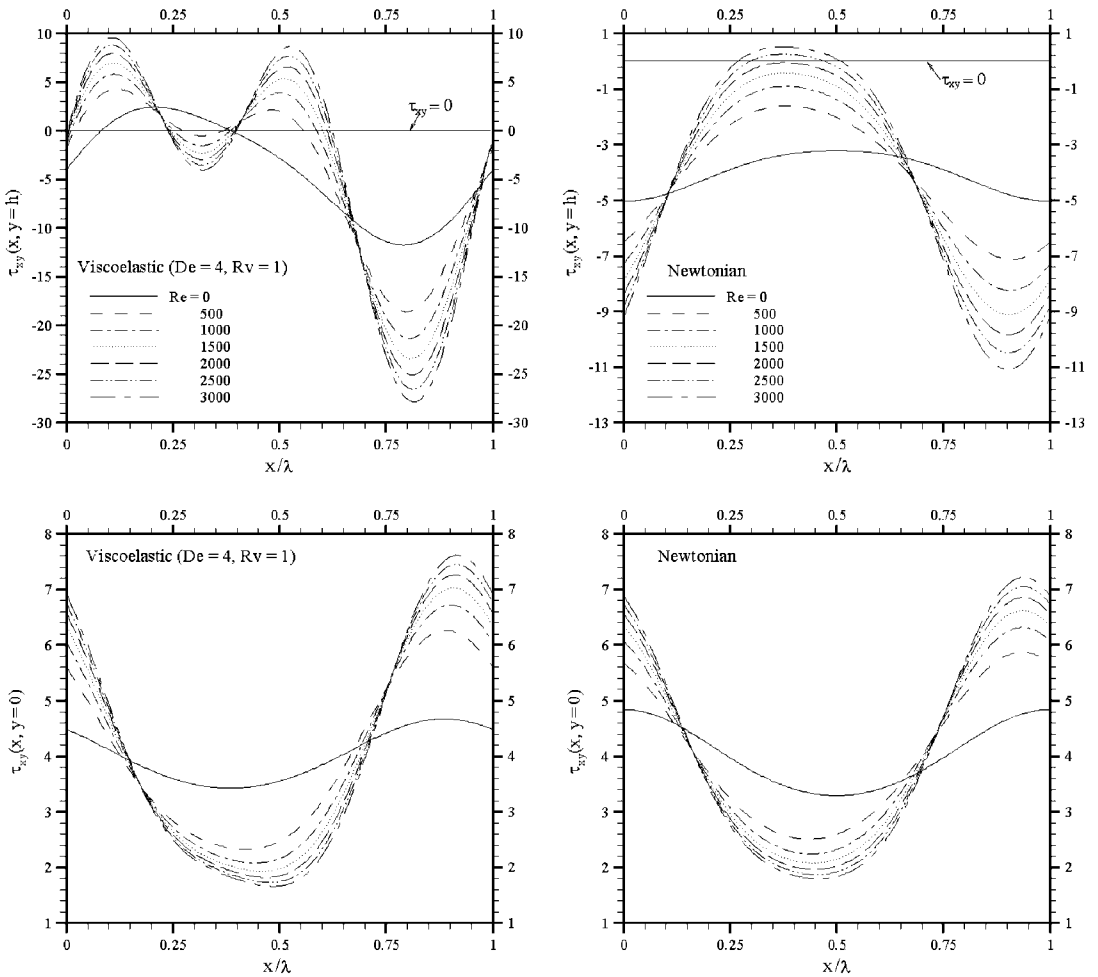

Figure 12. Inertia effects on the shear stress distribution, τ_{xy}, along the upper and lower walls for viscoelastic fluid ($De = 4$, $Rv = 1$), left, and Newtonian fluid, right. Here $\varepsilon = 0.1$ and $\alpha = 1$.

profiles near the lower wall for a viscoelastic fluid. Increasing inertia results in an increase in the magnitude of N. Furthermore, the N distribution along the lower wall is smoother in comparison with its distribution along the upper wall.

Figure 12 shows τ_{xy} profiles at the upper and lower walls for a viscoelastic fluid ($De = 4$, $Rv = 1$), and Newtonian fluid, for the range $Re \in [0, 3000]$. While inertia increases the magnitude of τ_{xy} for both fluids, the τ_{xy} distribution along the upper wall is dramatically altered as elasticity increases, resulting in the appearance of relative extrema at more locations. In other words, τ_{xy} changes sign more frequently for a viscoelastic fluid than for a Newtonian fluid near the upper wall. Comparison between τ_{xy} and N profiles (see Figure 11) near the upper wall for a viscoelastic fluid reveals that in the inertial regime the normal and shear stress extrema appear at almost the same locations. It is interesting to observe that although the flow

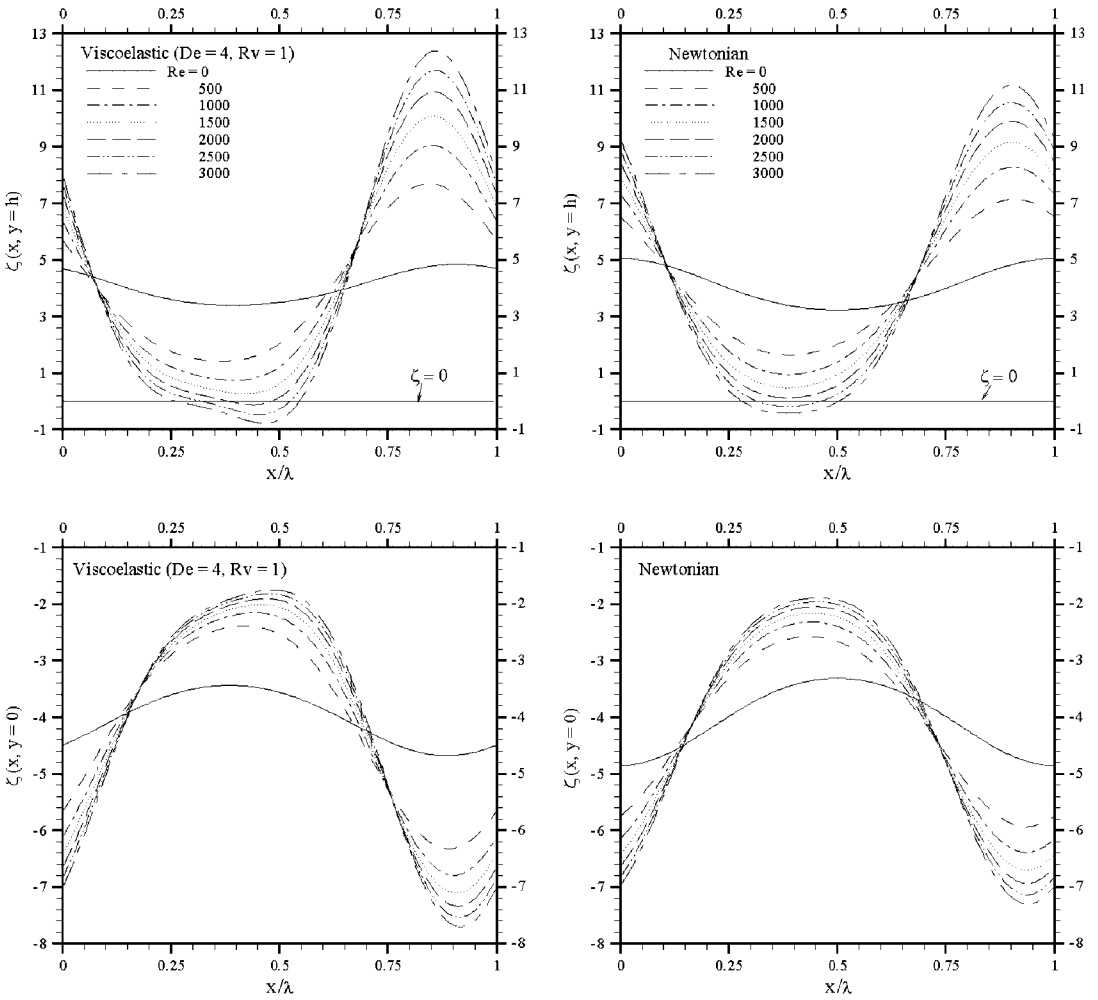

Figure 13. Inertia effects on vorticity distribution, ζ, along the upper and lower walls for viscoelastic fluid ($De = 4$, $Rv = 1$), left, and Newtonian fluid, right. Here $\varepsilon = 0.1$ and $\alpha = 1$.

kinematics is essentially the same for both Newtonian and viscoelastic fluids (see Figure 4), the stress distributions are dramatically different. Also, the separation and reattachment points for viscoelastic flow do not directly correspond to the change of τ_{xy} sign as in the case of a Newtonian flow due to the presence of extra stresses for a viscoelastic fluid. The insignificant effect of elasticity on τ_{xy} profiles near the lower wall in the inertial region is expected as explained earlier (see Figure 7 and Equation (17)).

In order to have a comprehensive view regarding the influence of inertia on viscoelastic flow through modulated channels, the variation of the vorticity, ζ, at the boundary should be addressed. Figure 13 displays ζ profiles at the upper and lower walls for viscoelastic ($De = 4$, $Rv = 1$), and Newtonian fluids, for the range $Re \in [0, 3000]$. For both fluids, inertia

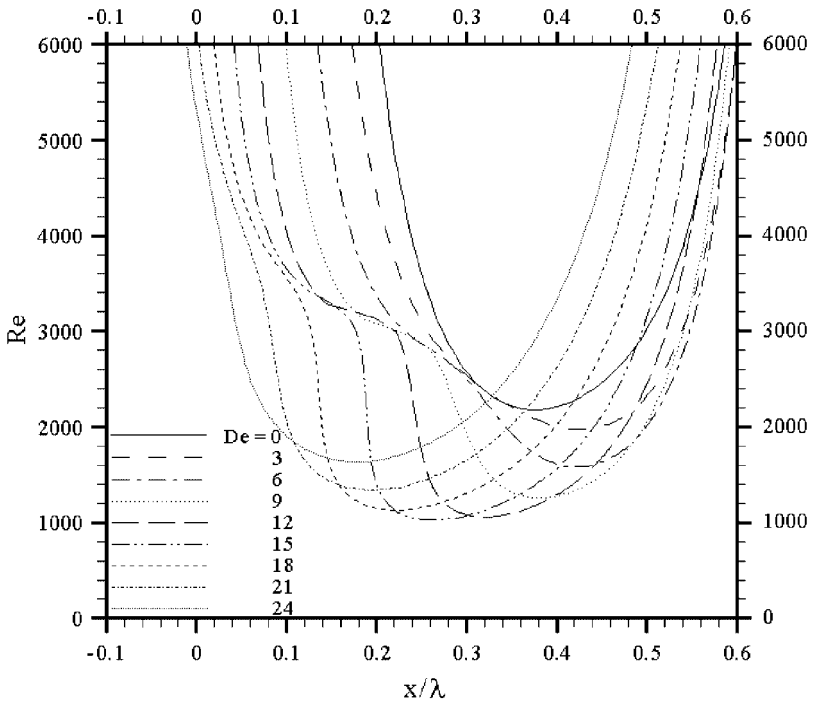

Figure 14. Influence of *De* on the locations of separation and reattachment points against Reynolds number, for $Rv = 1$, $\alpha = 1$, and $\varepsilon = 0.1$.

tends to cause ζ to switch sign along the upper wall, resulting in the onset of backflow at a critical Reynolds number, Re_c. This critical value depends on the fluid type. Separation will occur near the upper wall in the range $1500 < Re_c < 2000$ for a viscoelastic fluid and $2000 < Re_c < 2500$ for a Newtonian fluid. In other words, Re_c is smaller for a viscoelastic flow. Further increase in *Re* results in a larger vortex size. Viscoelastic flow is characterized by a larger vortex than the Newtonian flow for $Re > Re_c$. Viscoelastic flow vorticity profiles along the upper wall suggest that the vortex might go through sudden expansion as *Re* exceeds further beyond Re_c. Such behaviour is not observed for Newtonian fluid. Although it was demonstrated earlier that elasticity tends to minimize the effect of the modulation, making the flow behaves similar to that between two flat plates (see Figure 8), this observation is limited to creeping flow since inertia-dominated viscoelastic flows are characterized by a larger vortex size and a smaller Re_c. The ζ profiles along the lower wall are always negative. Thus, flow separation along the lower wall cannot be deduced for the range examined in this figure. However, one can still infer from the figure that backflow along the lower wall will eventually occurs below the crest as *Re* exceeds a different critical Reynolds number. This critical value depends on fluid elasticity. Figure 13 shows that along the lower wall the ζ magnitude for viscoelastic fluid is larger than that for Newtonian fluid. The threshold for the onset of backflow along the lower wall will be addressed later. Note the effect of elasticity on the ζ distribution. In the absence of inertia, elasticity shifts the maximum upstream. As inertia increases, elasticity causes a downstream shift in the maximum location.

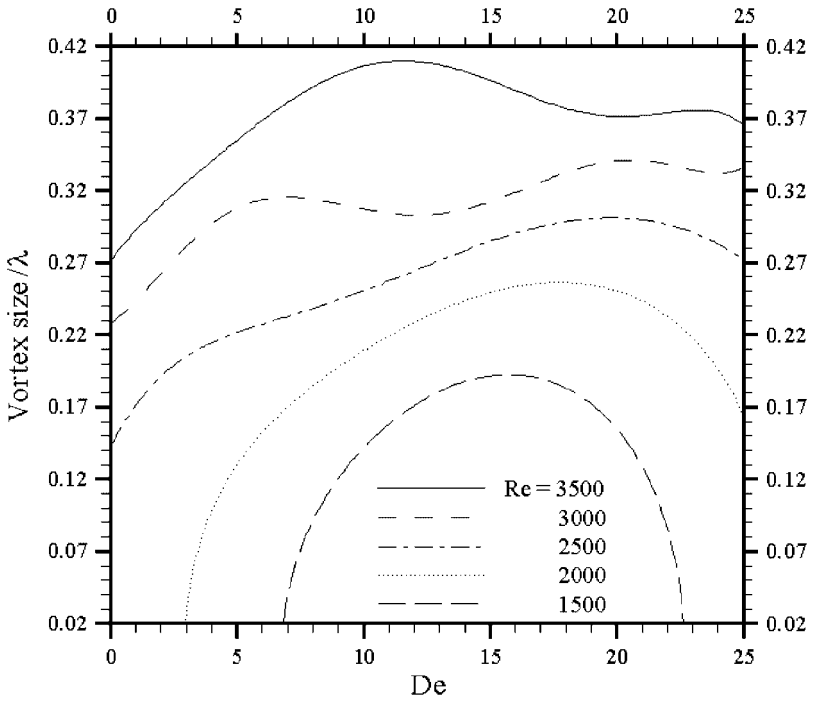

Figure 15. Influence of Re on the vortex size plotted against De, for $Rv = 1$, $\varepsilon = 0.1$ and $\alpha = 1$.

In sum, inertia dramatically alters stress and pressure distribution. Flow kinematics are also influenced by inertia. As Re exceeds a certain threshold, backflow occurs in the region of expansion (below the crest). This threshold is smaller for the viscoelastic fluid. However, earlier investigations demonstrated that in the absence of inertia, an increase in elasticity will result in a reduction in the vortex size for the flow through periodically sinusoidal periodic constricted tube with large amplitude, $\varepsilon = 0.5$, and $\alpha = \pi$ [3, 20]. In particular, they demonstrated that the crest symmetric vortex that occurred upon examining creeping Newtonian flow shifts downstream upon the introduction of elasticity and further increase in elasticity causes shrinkage in the vortex size (see Figures 9–11 in Reference [20], for example). However, these studies were limited to creeping flow and to a single channel configuration. Inertia and geometric parameters are expected to influence the conditions for the onset of backflow. Their effect on Re_c and the vortex formation will be examined next for viscoelastic fluids.

4.3. Interplay between inertia and viscoelastic effects, and backflow

The combined effect of elasticity and inertia is expected to influence the vortex size and location as well as the threshold for the onset of backflow. The quantitative effect of elasticity on the distance between separation and reattachment locations (*vortex size*) and vortex location has never been investigated in the inertial regime, and will be emphasized here. Figure 14 shows the location of the points of separation and reattachment as function of the Reynolds number, for $De \in [0, 24]$, $Rv = 1$, $\varepsilon = 0.1$ and $\alpha = 1$. At a given Re, the separation point lies to

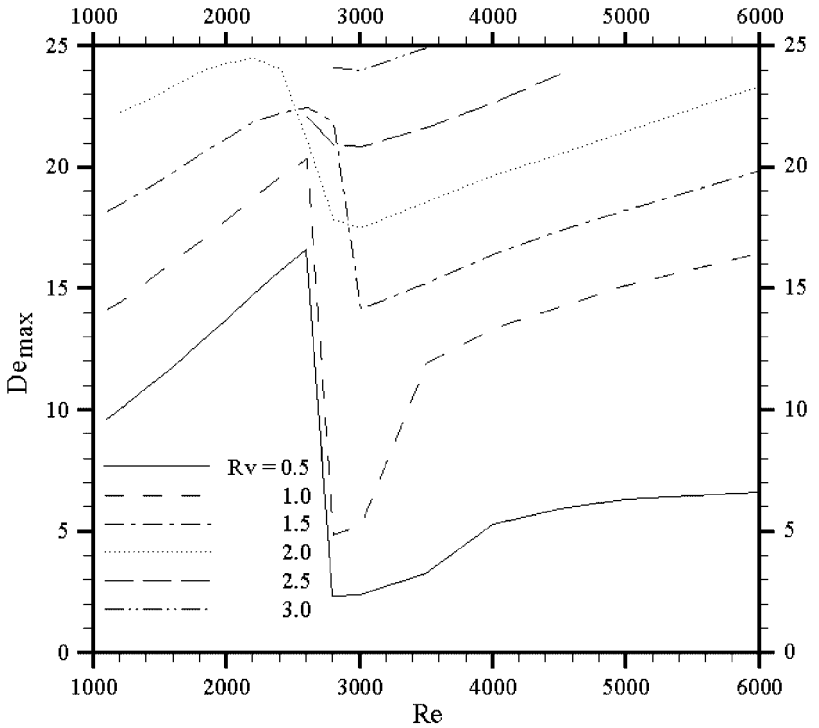

Figure 16. Influence of Rv on $De_{\max}$ as a function of Re for $\varepsilon = 0.1$ and $\alpha = 1$.

the left, and the reattachment point lies to the right. The critical Reynolds number for the onset of backflow, Re_c, which corresponds to the minimum point of each curve, depends significantly on De. In general, as Re increases above Re_c, the vortex size increases. The vortex centre does not coincide with the midpoint of the wall period; it is located, as expected, upstream of $x = \lambda/2$. While the point of separation moves upstream as De increases for a given Re, the location of the reattachment points vacillates with De. Furthermore, there is a sudden increase in the vortex size at $Re \approx 3100$ for the range $6 < De < 21$. Another interesting feature captured by this figure is the non-monotonic effect of De on Re_c. The non-monotonic influence of De is also reflected on the vortex location at the onset. Initially, elasticity causes a downstream shift in this location. As De increases above 4, the vortex location at the onset migrates upstream.

Figure 15 shows the change in vortex size as function of De for $Re \in [1500, 3500]$, $Rv = 1$, $\varepsilon = 0.1$, and $\alpha = 1$. For $Re \leqslant 2500$, the vortex size increase as De increases until De reaches a critical value, $De_{\max}$, at which the vortex reaches its maximum size for given Rv and Re. Clearly, at relatively low Re backflow exists only over a finite range of De values. For $Re > 2000$, backflow exists for all practical values of De. Simultaneously, the maximum weakens as Re increases, giving way to two mild maxima. Figure 16 shows the change in $De_{\max}$ as Re increases for $Rv \in [0.5, 3]$, $\varepsilon = 0.1$ and $\alpha = 1$. In this case, no backflow appears for $Re < 1000$. For a given Rv, $De_{\max}$ increases with Re, and experiences a sudden drop at a Re that is weakly dependent on Rv ($Re \approx 2800$). As Re increases further, $De_{\max}$ increases but at a

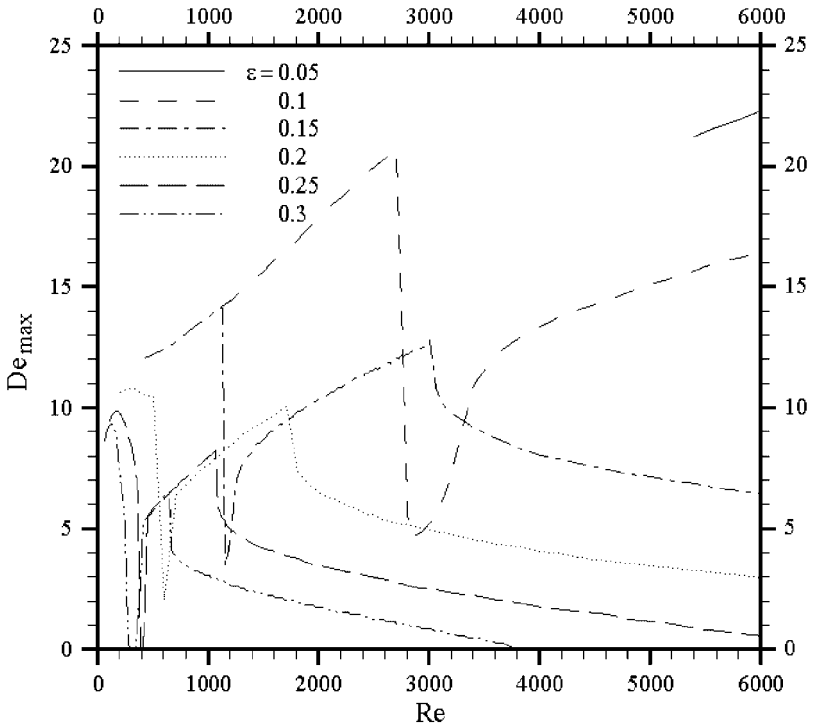

Figure 17. Influence of ε on $De_{\max}$ as a function of Re for $Rv = 1$ and $\alpha = 1$.

smaller rate with Re. As expected, $De_{\max}$ increases with Rv. Influence of geometric parameters on $De_{\max}$ is illustrated in Figures 17 and 18. Figure 17 shows the change in $De_{\max}$ as Re increases for $\varepsilon \in [0.5, 3]$, $\alpha = 1.0$ and $Rv = 1$. For a given ε, $De_{\max}$ increases as Re increases, and experiences a sudden drop at a Reynolds number that decreases with ε. As Re increases further, $De_{\max}$ increases and then decreases. As expected, $De_{\max}$ decreases with ε. Figure 18 shows the change in $De_{\max}$ as Re increases for $\alpha \in [0.8, 1.4]$, $\varepsilon = 0.1$ and $Rv = 1$. For a given α, $De_{\max}$ increases as Re increases, and experiences a sudden drop at a Re that decreases as α increases. As Re increases further, $De_{\max}$ increases. As expected, $De_{\max}$ decreases with α, which explains the absence of $De_{\max}$ for $\alpha < 0.8$.

The most important threshold parameter in the problem is Re_c, which is expected to depend on geometric and fluid parameters. Figure 19 shows the influence of Rv on Re_c, and corresponding vortex location, x_c/λ, as functions of De for $\varepsilon = 0.1$ and $\alpha = 1$. This is an important figure as it summarizes the interplay between inertia and elasticity. As expected, Re_c and x_c/λ approach the Newtonian limits for large Rv. Generally, Re_c decrease with De, and reaches a minimum at $De = De_{\max}$, corresponding to the maximum in vortex size (see Figure 16). The effect of elasticity is even stronger on the vortex location at the onset. Initially, the vortex shifts downstream as De increases until it reaches a critical position at De other than $De_{\max}$. The vortex location shifts upstream as De further increases. As Rv increases, the variation of vortex location with elasticity becomes smoother. The downstream shift of the vortex location

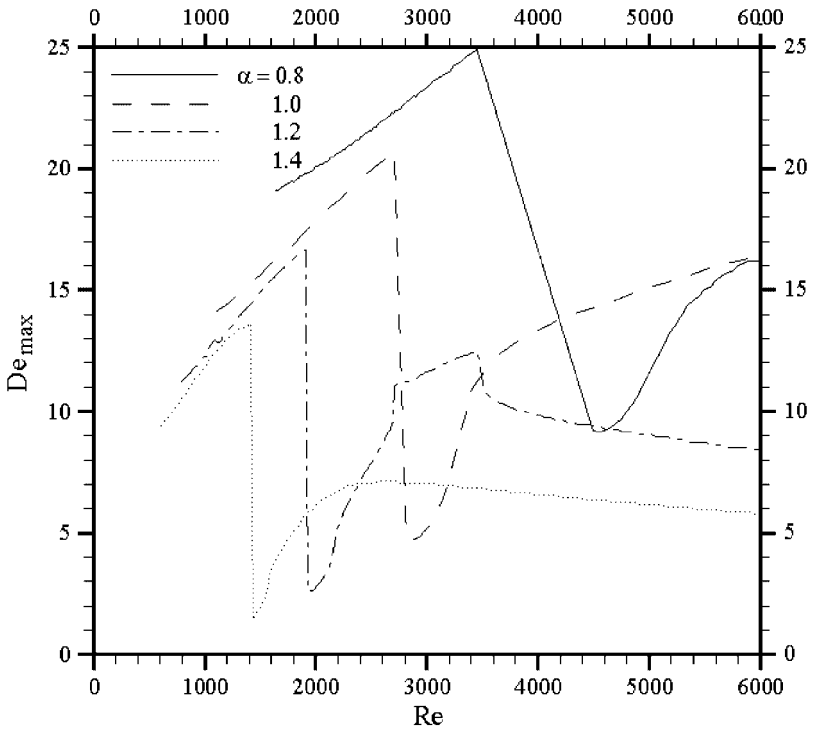

Figure 18. Influence of α on $De_{\max}$ as a function of Re for $Rv = 1$ and $\alpha = 1$.

for small values of elasticity is similar to the trend predicted by Pilitsis and Beris [3] and Burdette *et al.* [20] for creeping flow.

4.4. Backflow along the lower wall

Figure 20 illustrates the streamlines, pressure and normal stress contours for two viscoelastic fluids, $De = 4$ (Figure 20(a)) and $De = 8$ (Figure 20(b)). Here $Re = 2500$, $Rv = 1$, $\alpha = 1$ and $\varepsilon = 0.2$. Wall amplitude influence on the flow topology is inferred upon comparing Figure 20(a) and Figure 9 for $\varepsilon = 0.2$ and 0.1, respectively (the remaining parameters are the same). An increase in the wall amplitude results in an increase in the vortex size. The vortex doubles its size as ε increases from 0.1 to 0.2. The increase in the vortex size is associated with the increase in the adverse (streamwise) pressure gradient as ε increases. The increase in the pressure gradient is evident from the increase in the pressure magnitude while the pressure profiles along the walls remain relatively unchanged as ε increases. The influence of the wall amplitude on the stress distribution is inferred from the contours of normal stress difference, N. Comparison between Figures 9 and 20(a) shows that larger wall amplitude results in larger N magnitudes near the walls. This increase in magnitude is accompanied by sharper stress gradients along the walls.

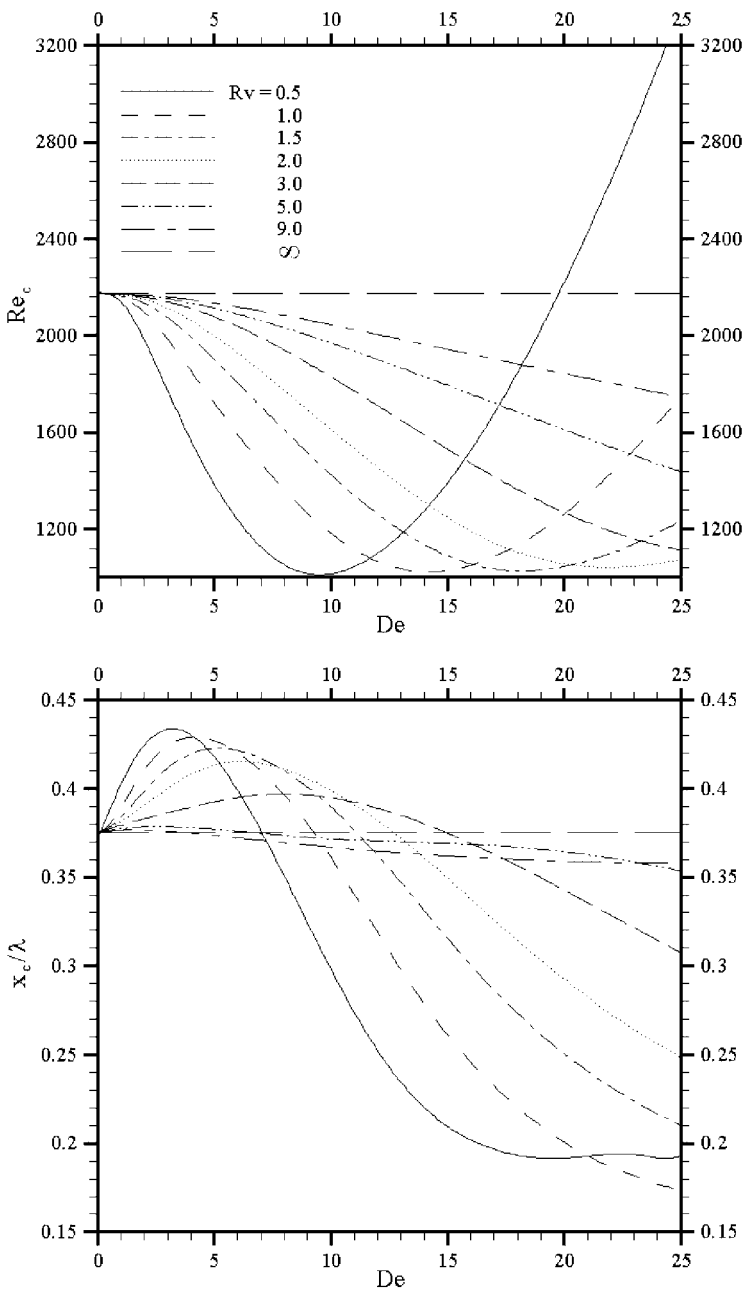

Figure 19. Influence of Rv on the critical Reynolds number for the onset of backflow, Re_c, and the vortex centre location, x_c/λ, plotted against De, for $\varepsilon = 0.1$ and $\alpha = 1$.

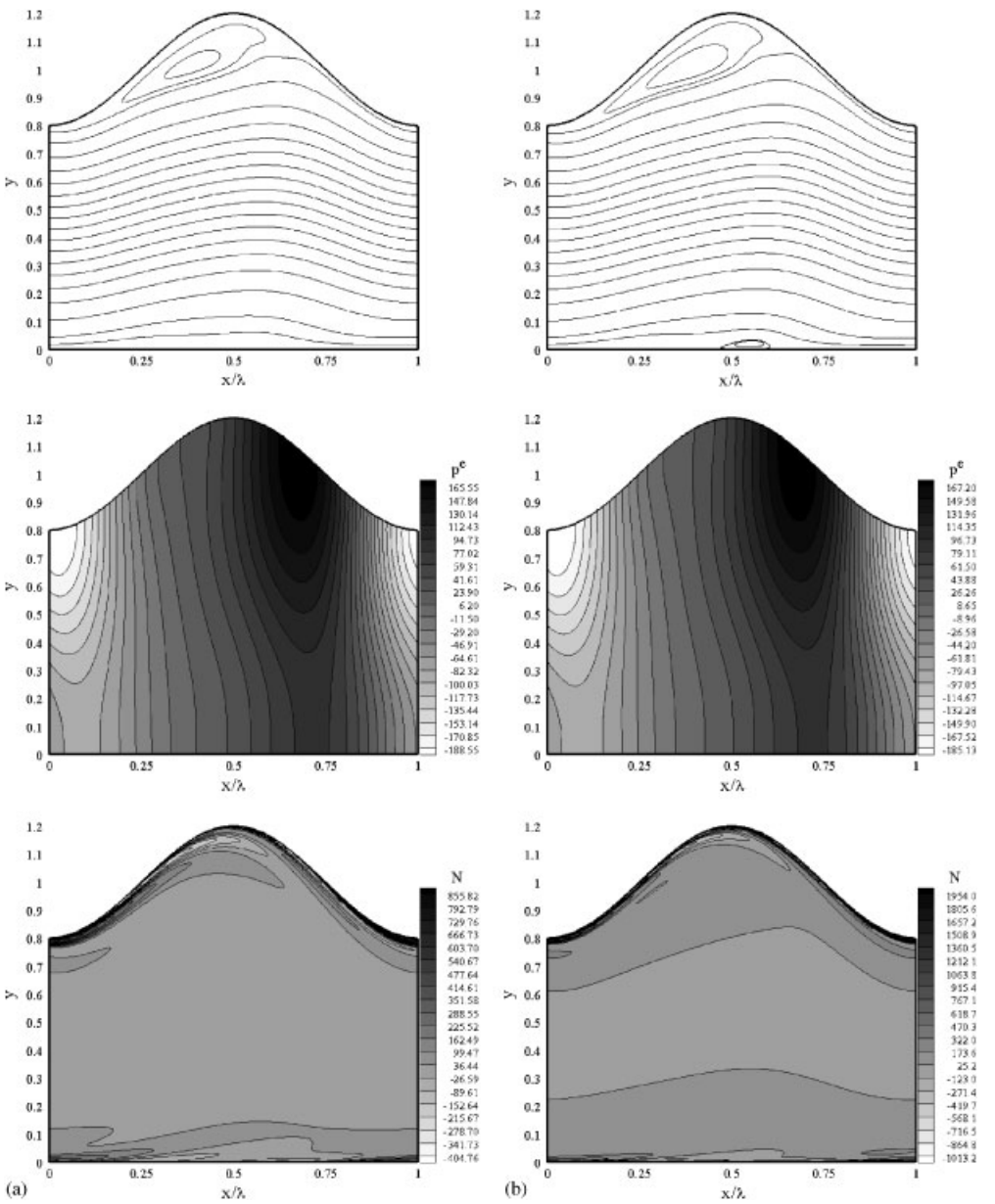

Figure 20. Influence of elasticity on the flow response for a modulated channel with larger amplitude ($\varepsilon = 0.2$, $\alpha = 1$). The figure displays streamlines, pressure departure, p^e, and the contours of the normal stress difference, N, for (a) $De = 4$ and $Rv = 1$, and (b) $De = 8$ and $Rv = 1$.

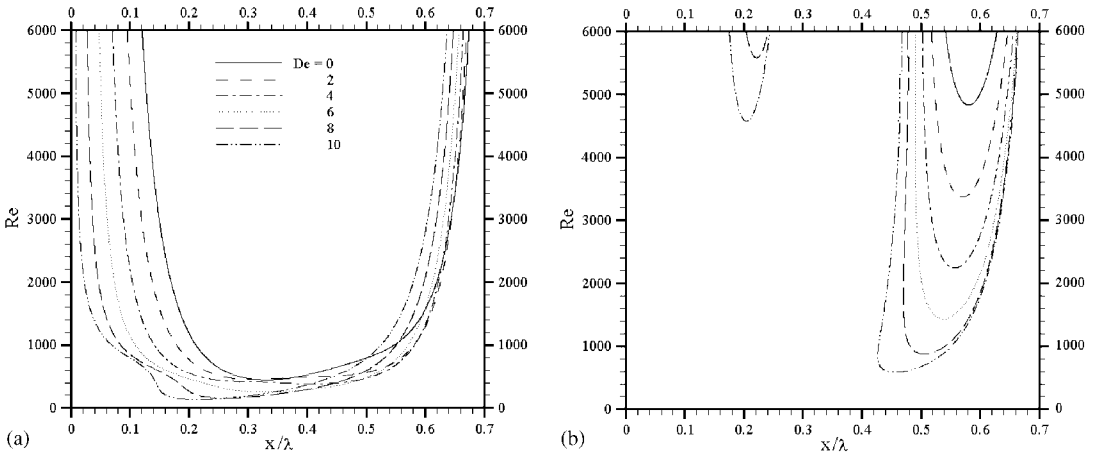

Figure 21. Influence of De on the locations of separation and reattachment points against the Reynolds number for, for $Rv = 1$, $\alpha = 1$, and $\varepsilon = 0.2$ at the upper wall, $y = h$ (a), and lower wall, $y = 0$ (b).

Another effect of ε on the flow kinematics is the significant loss of symmetry near the lower wall as illustrated for $\varepsilon = 0.2$ in Figure 20(a). This loss of symmetry indicates that a secondary flow region develops near the lower wall by changing the controlling parameters. Evidence of vortex formation near the lower wall is illustrated when De increases from 4 to 8 as depicted in Figure 20. The lower wall vortex appears in the region $x/\lambda \in [0.48, 0.65]$. The lower wall vortex is much smaller than the upper wall vortex. The smaller vortex size near the lower wall can be correlated with the smaller streamwise pressure gradient along the lower wall in comparison with the upper wall. Further comparison between Figures 20(a) and (b) shows that although elasticity has negligible effect on the pressure, it dramatically alters the normal stress magnitudes and distribution. This is in agreement with the results reported above (see Figures 5, 6, 9–11).

Figure 21 shows the location of separation and reattachment points at the upper wall (Figure 21(a)) and lower wall (Figure 21(b)) as functions of the Reynolds number, for $De \in [0, 10]$, $Rv = 1$, $\varepsilon = 0.2$ and $\alpha = 1$. At the upper modulated wall, comparison with Figure 14 shows that Re_c decreases as ε increases. Furthermore, the vortex size along the upper wall is typically larger for $\varepsilon = 0.2$. Thus, the Re versus x/λ curve exhibit weaker minimum as ε increases. This is similar to the wall modulation effect on vortex formation for a typical Newtonian fluid [1, 12–14, 31, 35, 37]. For the examined elasticity range, backflow near the lower wall emerges downstream of the crest. The critical Reynolds number for the onset of backflow near the lower wall, Re_{cl}, which corresponds to the minimum point of each curve, depends significantly on De. Comparison between Figures 21(a) and (b) reveals that along the lower wall the Re versus x/λ curve is narrower, exhibiting a strong minimum, from which Re_{cl} is easily identified. As Re increases beyond Re_{cl}, a second vortex near the lower wall appears in the diverging section of the channel for highly elastic fluids. The appearance of the secondary vortex can be related to the fluctuation in the vorticity profiles along the lower wall. It is interesting to notice the appearance of small vortex along the lower wall for Newtonian

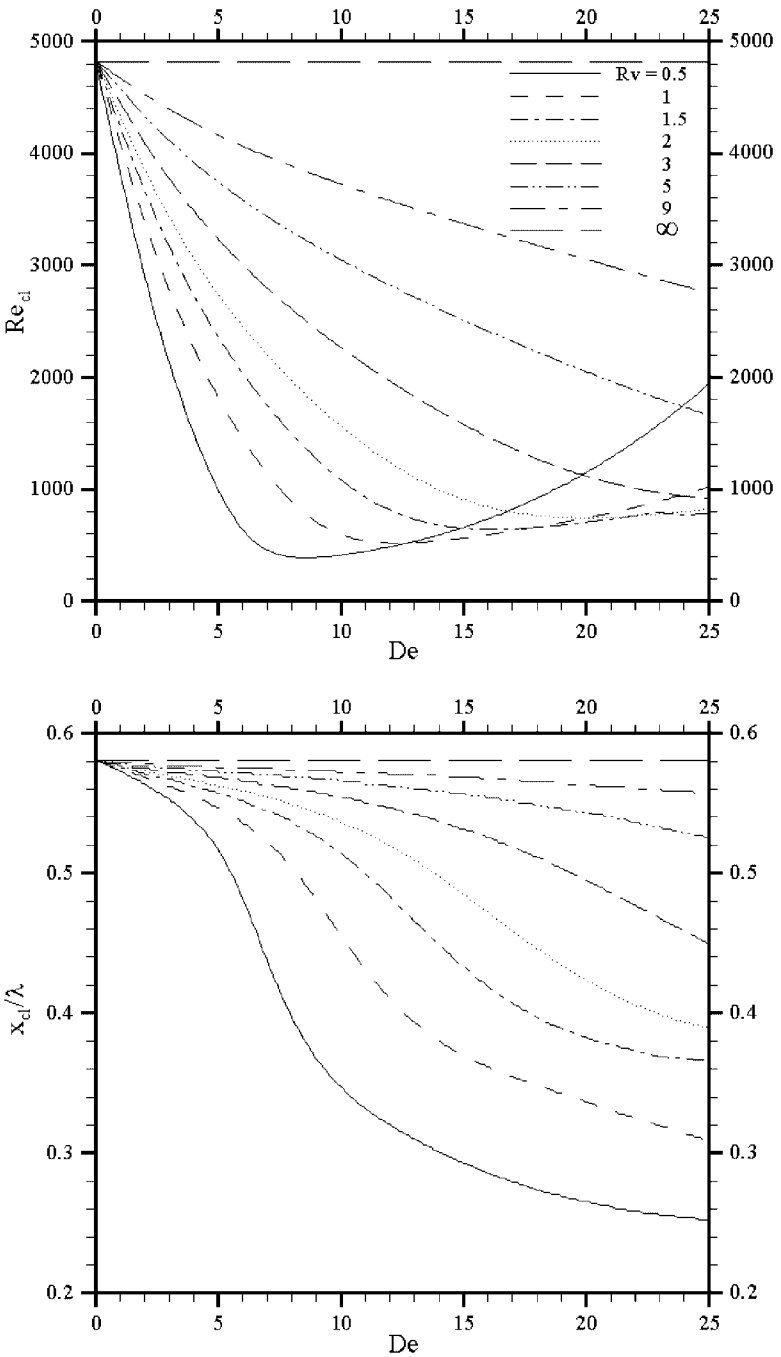

Figure 22. Influence of Rv on the critical Reynolds number for the onset of backflow along the lower wall, Re_{cl}, and the vortex centre location, x_{cl}/λ, plotted against De, for $\varepsilon = 0.2$ and $\alpha = 1$.

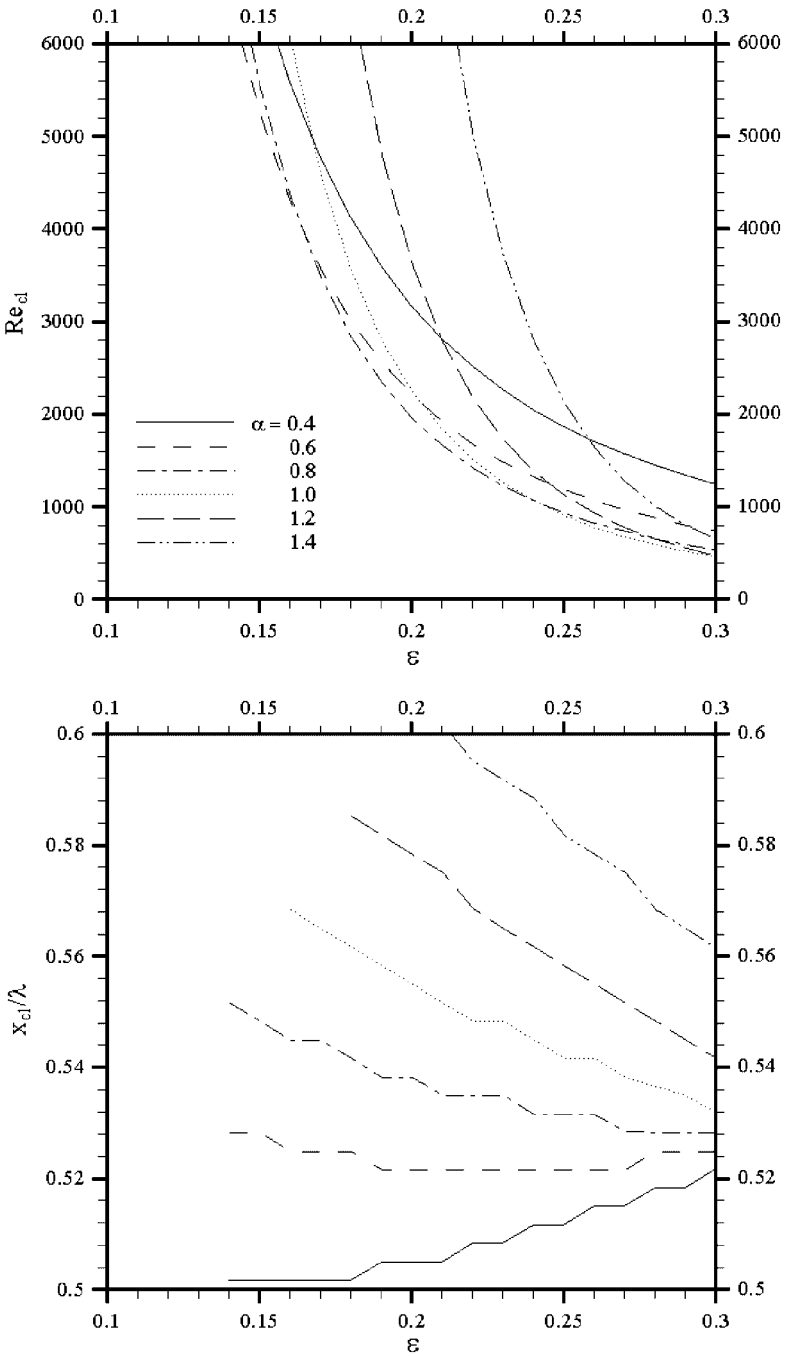

Figure 23. Influence of the wall modulation wavenumber on the critical Reynolds number for the onset of backflow at the lower wall, Re_{cl}, and the vortex location against the modulation amplitude, ε, for a viscoelastic fluid, $De = 4$, $Rv = 1$.

flow with relatively high Reynolds number. This is not surprising since it was established earlier that inertia contributes to a significant increase in the pressure gradient near both walls (see Figure 9). A large pressure gradient would force separation to occur, which is consistent with the present result.

Viscoelastic effects on the flow kinematics can be further explored upon examination of the critical conditions for the onset of backflow near the straight wall. Figure 22 shows the influence of Rv on the critical Reynolds number, Re_{cl}, and corresponding vortex location, x_{cl}/λ, at the onset of backflow along the lower wall, as functions of De for $\varepsilon = 0.2$ and $\alpha = 1$. As expected, Re_{cl} and x_{cl}/λ approach the Newtonian limit as Rv increases. Generally, Re_{cl} decrease with De, and reaches a minimum at a critical De that increases as Rv increases. Above this critical De, Re_{cl} increases with De. Elasticity effects are even stronger on the vortex location at the onset. In general, the vortex location travels upstream as De increases.

Wall modulation amplitude and wavelength are expected to strongly affect the critical conditions for the onset of backflow near the lower wall. Figures 23(a) and (b) illustrate the influence of α on the dependence of Re_{cl} and x_{cl}/λ, respectively, on ε for a typical viscoelastic fluid, $De = 4$ and $Rv = 1$. Although Re_{cl} decreases exponentially as ε increases, α has a non-monotonic effect on Re_{cl}. A critical wavenumber above which an increase in α results in a simultaneous growth in Re_{cl} exists. Further calculations show that the critical α is related to the fluid type. In particular, as Rv increases, the critical α decreases. Earlier experimental and numerical investigations [15, 51–53] on Newtonian flow on similar geometries fail to report any backflow near the flat wall simply because of the large wavenumber, $\alpha = 2\pi$, used in those studies. For the examined viscoelastic fluid, a universal relation among Re_{cl}, ε, and α could not be identified. The vortex location at the onset is altered by α. For small α, an increase in ε leads to a minor downstream shift in the vortex location. For $\alpha > 0.6$, an increase in ε leads to a very small upstream shift in the vortex location. The critical location curves seem to converge towards a critical value ($x_{cl}/\lambda \approx 0.53$).This convergence is expected and it correlates to the convergence of Re_{cl} towards the zero limit. It is interesting to notice a saturation effect of the wall modulation amplitude on the vortex location for some ranges of ε. In other words, the vortex location changes with ε in a *staircase* like behaviour. This behaviour is correlated to the wall modulation amplitude effect on the pressure distribution along the lower wall. While elasticity alters the extrema pressure location along the lower as clearly illustrated in Figure 5, the wall modulation amplitude does not seem to have a noticeable effect on the loci of the extrema as depicted from the comparison between Figures 20(a) and 9. Comparison between Figures 22 and 23 further supports the insignificant influence of ε on x_{cl}/λ. While x_{cl}/λ shifts upstream from 0.58 to 0.31 as De increases from 0 to 25 for $Rv = 1$, $\varepsilon = 0.2$, and $\alpha = 1$, x_{cl}/λ changes from 0.57 to 0.53 as ε increases from 0.15 to 0.3 for $Rv = 1$, $De = 4$, and $\alpha = 1$. A similar staircase phenomenon is expected to occur along the upper wall as indicated by Figure 12 in Reference [13] for the Newtonian limit.

5. CONCLUDING REMARKS

The interplay between inertial and viscoelastic effects is examined in this study, for the flow in spatially weakly modulated channels. A perturbation approach is applied to obtain the flow field and stresses. A comparative assessment is carried out against experimental results for Newtonian flow. Influence of viscoelastic parameters on the range of validity of the method

is also assessed on the basis of conservation of mass. It is established that the perturbation approach is globally valid to within the highest-order terms kept in the expansion of velocity and pressure (which, in this case is ε^3). The main advantage of the perturbation solution is its ease in implementation, and the low CPU and storage requirement, compared to a full finite-volume or finite-element simulation.

The influence of inertia, viscoelastic parameters, modulation amplitude and wavelength on the flow through spatially modulated channel is emphasized. In particular, the influence of these parameters on conditions for the onset of vortex flow, vortex size and location is systematically examined. Non-monotonic dependence of the vortex size on elasticity is reported. A critical De, $De_{\max}$, above which elasticity results in a smaller vortex has been identified. A relation between $De_{\max}$ and flow parameters has been established here. This relation is important as it clarifies the role of elasticity in the light of earlier contradictory results reported on the effect of elasticity on vortex formation [3, 18, 20]. It is found that backflow also emerges near the lower straight wall as well. Backflow near the wall was not observed in previous experimental studies [15, 51–53] because of the relatively large wavenumber modulation used. The threshold for the onset of backflow near the lower or the upper wall was established. In general, the critical Re for the onset of backflow near the lower wall, Re_{cl}, is much smaller than the critical Re for the onset of backflow near the upper wall, Re_{c}. It is found that Re_{c} or Re_{cl} initially decrease with De and eventually level off or even increase as De exceeds a critical value. Similar to Newtonian flow, an increase in the wall amplitude leads to a larger vortex size and a smaller critical Reynolds number for the onset of backflow at either wall.

ACKNOWLEDGEMENTS

The work is supported by the Natural Sciences and Engineering Research Council of Canada.

REFERENCES

1. Sobey IJ. On the flow through furrowed channels. Part 1: calculated flow patterns. *Journal of Fluid Mechanics* 1980; **96**:1–26.
2. Pilitsis S, Beris AN. Calculation of steady-state viscoelastic flow in an undulating tube. *Journal of Non-Newtonian Fluid Mechanics* 1989; **31**:231–287.
3. Pilitsis S, Beris AN. Viscoelastic flow in an undulating tube. Part II. Effects of high elasticity, large amplitude of undulation and inertia. *Journal of Non-Newtonian Fluid Mechanics* 1991; **39**:375–405.
4. Pilitsis S, Souvaliotis A, Beris AN. Viscoelastic flow in a periodically constricted tube: the combined effect of inertia, shear thinning and elasticity. *Journal of Rheology* 1991; **35**:605–646.
5. Beris AN, Avgousti M, Souvaliotis A. Spectral calculation of viscoelastic flows: evaluation of Giesekus constitutive equation in model flow problems. *Journal of Non-Newtonian Fluid Mechanics* 1992; **44**:197–228.
6. Dieber JA, Schowalter WR. Modeling the flow of viscoelastic fluids through porous media. *AIChE Journal* 1981; **27**:912–920.
7. Phan-Thien N, Khan MMK. Flow of an Oldroyd-type fluid through a sinusoidally corrugated tube. *Journal of Non-Newtonian Fluid Mechancis* 1987; **24**:203–220.
8. Zheng R, Phan-Thien N, Tanner RI, Bush MB. Numerical analysis of viscoelastic flow through a sinusoidally corrugated tube using a boundary element method. *Journal of Rheology* 1990; **34**:79–102.
9. Hurarewicz H, Gupta RK, Chaabra RP. Elastic effects in flow of fluids through sinuous tubes. *Journal of Rheology* 1991; **35**:221–235.
10. Yalamanchili RC. Flow of Non-Newtonian fluids in corrugated channels. *International Journal of Non-Linear Mechanics* 1993; **28**:535–548.
11. Yalamanchili RC, Sirivat A, Rajagopal KR. An experimental investigation of the flow of dilute polymer solutions through corrugated channels. *Journal of Non-Newtonian Fluid Mechanics* 1995; **58**:243–277.
12. Leneweit G, Auerbach D. Detachment phenomena in low Reynolds number flows through sinusoidally constricted tubes. *Journal of Fluid Mechanics* 1999; **387**:129–150.

13. Zhou H, Khayat RE, Martinuzzi RJ, Straatman AG. On the validity of the perturbation approach for the flow inside weakly modulated channels. *International Journal for Numerical Methods in Fluids* 2002; **39**:1139–1159.
14. Zhou H, Martinuzzi RJ, Khayat RE, Straatman AG, Abu-Ramadan E. Influence of wall shape on vortex formation in modulated channel flow. *Physics of Fluids* 2003; **15**:3114–3133.
15. Günther A, von Rohr PR. Large-scale structures in a developed flow over a wavy wall. *Journal of Fluid Mechanics* 2003; **478**:257–285.
16. Stüer H. Investigation of separation on a forward facing step. *Ph.D. Thesis*, Swiss Federal Institute of Technology (ETH), Diss. ETH No. 13132, 1999.
17. Davidson DL, Graessley WW, Schowalter WR. Velocity Stress fields of polymeric liquids in a periodically constricted channel. Part 1. Experimental methods and straight channel validations. *Journal of Non-Newtonian Fluid Mechanics* 1993; **49**:317–344.
18. Rothstein JP, McKinley GH. Extensional flow of a polystyrene Boger fluid through a 4:1:4 axisymmetric contraction/expansion. *Journal of Non-Newtonian Fluid Mechanics* 1999; **86**:61–88.
19. Davidson DL, Graessley WW, Schowalter WR. Velocity stress fields of polymeric liquids in a periodically constricted channel. Part 2. Observation of non-Newtonian behaviour. *Journal of Non-Newtonian Fluid Mechanics* 1993; **49**:345–375.
20. Burdette SR, Coates PJ, Armstrong RC, Brown RA. Calculation of viscoelastic flow through an axisymmetric corrugated tube using the explicitly elliptic momentum equation formulation. *Journal of Non-Newtonian Fluid Mechanics* 1989; **33**:1–23.
21. Marshall RJ, Metzner AB. Flow of viscoelastic fluids through porous media. *Industrial and Engineering Chemistry Fundamentals* 1967; **6**:393–403.
22. Skartsis L, Khomami B, Kardos JL. Polymeric flow through fibrous media. *Journal of Rheology* 1992; **36**: 589–620.
23. Talwar KK, Khomami B. Flow of viscoelastic fluids past periodic square arrays of cylinders: inertial and shear thinning viscosity and elasticity effects. *Journal of Non-Newtonian Fluid Mechanics* 1995; **57**:177–202.
24. James DF, Phan-Thien N, Khan MMK, Beris AN, Pilitsis S. Flow of test fluid M1 in corrugated tubes. *Journal of Non-Newtonian Fluid Mechanics* 1990; **35**:405–412.
25. Crochet MJ, Delvaux V, Marchal JM. On the convergence of the streamline-upwind mixed finite element. *Journal of Non-Newtonian Fluid Mechanics* 1990; **34**:261–268.
26. Skartsis L. The permeation of fiber beds by Newtonian and non-Newtonian fluids with applications to the autoclave and resin transfer molding processes. *D.Sc. Dissertation*, Sever Institute of Technology, Washington University, St. Louis, MO, 1992.
27. Sureshkumar R. Local linear stability characteristics of viscoelastic periodic channel flow. *Journal of Non-Newtonian Fluid Mechanics* 2001; **97**:125–148.
28. Doyle PS, Shaqfeh ESG, McKinely GH, Spiegelberg SH. Relaxation of dilute polymer solutions following extensional flow. *Journal of Non-Newtonian Fluid Mechanics* 1998; **76**:79–110.
29. Hinch EJ. Uncoiling a polymer molecule in a strong extensional flow. *Journal of Non-Newtonian Fluid Mechanics* 1994; **54**:209–230.
30. Rallison JM. Dissipative stresses in dilute polymer solutions. *Journal of Non-Newtonian Fluid Mechanics* 1997; **68**:61–83.
31. Stephanoff KD, Sobey IJ, Bellhouse BJ. On flow through furrowed channels. Part 2: observed flow patterns. *Journal of Fluid Mechanics* 1980; **96**:27–32.
32. Tsangaris S, Leiter E. On laminar steady flow in sinusoidal channels. *Journal of Engineering Mathematics* 1984; **18**:89–103.
33. Nishimura T, Ohoriand Y, Kawamura Y. Flow characteristics in a channel with symmetric wavy wall for steady flow. *Journal of Chemical Engineering of Japan* 1984; **17**:466–471.
34. Nishimura T, Murakami S, Arakawa S, Kawamura Y. Flow observations and mass transfer characteristics in symmetrical wavy-walled channels at moderate Reynolds numbers for steady flow. *International Journal of Heat and Mass Transfer* 1990; **33**:835–845.
35. Selvarajan S, Tulapurkara EG, Vasanta Ram V. A Numerical study of flow through wavy-walled channels. *International Journal for Numerical Methods in Fluids* 1998; **26**:519–531.
36. Guzman AM, Amon CH. Flow patterns and forced convective heat transfer in converging–diverging channels. *ASME HTD* 1993; **237**:43–53.
37. Lahbabi A, Chang HC. Flow in periodically constricted tubes: transition to inertial and nonsteady flows. *Chemical Engineering Science* 1986; **41**:2487–2505.
38. Nishimura T, Ohoriand Y, Kajimoto Y, Kawamura Y. Mass transfer characteristics in a channel with symmetric wavy wall for steady flow. *Journal of Chemical Engineering of Japan* 1985; **18**:550–555.
39. Keunings R. Simulation of viscoelastic fluid flow. In *Fundamentals of Computer Modeling for Polymer Processing*. Tucker III CL (ed.). Carl Hanse Verlag: Berlin, 1988.
40. Marchal JM, Crochet MJ. A new mixed finite element for calculating viscoelastic flow. *Journal of Non-Newtonian Fluid Mechanics* 1987; **20**:77–114.

41. King RC, Apelian MR, Armstrong RC, Brown RA. Numerically stable finite-element techniques for viscoelastic calculations in smooth and singular geometries. *Journal of Non-Newtonian Fluid Mechanics* 1988; **29**:147–216.
42. Chmielewski C, Jayaraman K. Elastic instability in crossflow of polymer solutions through periodic arrays of cylinders. *Journal of Non-Newtonian Fluid Mechanics* 1993; **48**:285–301.
43. Ahrens M, Yoo YJ, Joseph DD. Hyperbolicity and change of type in the flow of viscoelastic fluids through pipes. *Journal of Non-Newtonian Fluid Mechanics* 1987; **24**:67–83.
44. El-Soukkary TM, Straatman AG. The prediction of spatially periodic flows using a finite-volume model. *International Journal for Numerical Methods in Fluids* 2003; **41**:303–317.
45. Abu-Ramadan E, Khayat RE. Shear-thinning flow in weakly modulated channels. *International Journal for Numerical Methods in Fluids* 2005; **48**:467–499.
46. Bird RB, Armstrong RC, Hassager O. *Dynamics of Polymeric Liquids*, vol. 1. Wiley: New York, 1987.
47. Bruce C, Schwarz WH. Rheological properties of ionic and nonionic polyacrylamide solutions. *Journal of Polymer Science*. Part A-2-Polymer Physics 1969; **7**:909–927.
48. Abu Ramadan E. Channel flow and heat transfer of Newtonian and non-Newtonian fluids. *Ph.D. Thesis*, University of Western Ontario, 2005.
49. Prilutski G, Gupta RK, Sridhar T, Ryan ME. Model viscoelastic liquids. *Journal of Non-Newtonian Fluid Mechanics* 1983; **12**:233–241.
50. Jackson KP, Walters K, Williams RW. A rheometric study of Boger fluids. *Journal of Non-Newtonian Fluid Mechanics* 1984; **14**:173–188.
51. Hudson JD, Dykhno L, Hanaratty TJ. Turbulence production in flow over a wavy wall. *Experiments in Fluids* 1996; **20**:257–265.
52. Tanda G, Vittori C. Fluid flow and heat transfer in a two-dimensional wavy channel. *Heat and Mass Transfer* 1996; **31**:411–418.
53. Cherukat P, Na Y, Hanratty TJ, Mclaughlin JB. Direct numerical simulation of a fully developed turbulent flow over a wavy wall. *Theoretical and Computational Fluid Dynamics* 1998; **11**:109–134.

